NEUROSCIENCE

Coding principles of dopaminergic transmission modes

Limeng Huang[1], Yuanyu Chang[2], Zhipeng Yang[1], Wendy J. Lynch[3], B. Jill Venton[2]*

Dopaminergic neurons influence diverse behaviors with varied firing patterns, yet the precise mechanisms remain unclear. We introduce a multiplexed genetically encoded sensor–based imaging and voltammetry method to simultaneously record synaptic, perisynaptic, and extrasynaptic dopaminergic transmission at mouse central neurons. Using this method alongside a genetically encoded sensor–based image analysis program, we found that heterogeneous dopaminergic firing patterns create various transmission modes, encoding frequency, number, and synchrony of firing pulses using neurotransmitter quantity, releasing synapse count, and synaptic and/or volume transmission. Under both tonic and low-frequency phasic activities, transporters effectively reuptake dopamine at perisynaptic sites, confining dopamine within synaptic clefts to mediate synaptic transmission. In contrast, under high-frequency, particularly synchronized firing activity or transporter inhibition, released dopamine may overwhelm transporters, escaping from synaptic clefts via one to three outlet channels, triggering volume transmission. Our study illuminates a collaborative mechanism of synaptic enclosures, properties, and transporters that defines the coding principles of activity pattern–dependent dopaminergic transmission modes.

INTRODUCTION

Dopamine influences diverse human behaviors and diseases, yet it remains unclear whether the varied firing patterns of midbrain dopaminergic neurons support multiple distinct dopaminergic transmission modes that lead to specific modulations in behaviors and diseases (*1*–*4*). The early identification of distinct firing modes—tonic and burst patterns—in dopaminergic neurons inspired the idea that switching between these modes enables the modulation of dopamine release and signals, cooperating with diverse behavioral functions (*5*, *6*). The discovery of additional firing modes associated with various behaviors, such as wakefulness, alertness, and responses to punishment, small to medium and large rewards, and salient stimuli, reinforced this concept (*7*–*10*). However, because of limitations in dopamine monitoring techniques, comprehending how diverse firing modes translate into dopaminergic transmission modes and behavioral functions has proven more challenging than expected. Current models, based primarily on low–spatial resolution voltammetry experiments that detect typically only extracellular signals, propose dopamine as a volume transmitter, influencing many neighboring cells, largely irrespective of firing patterns. Moreover, the voltammetric experiments offered evidence of dopamine transporter (DAT) inhibition, enhancing dopamine diffusion and extracellular dopamine levels (*11*, *12*). This observation prompted a tacitly accepted, albeit pharmacologically counterintuitive, notion of transporter involvement in dopamine release regulation (*13*, *14*). In contrast, a couple of electrophysiology studies reported remarkably restrained dopaminergic transmission despite variations in estimates arising presumably from the reliance on indirect calculations and simulation assumptions (*15*, *16*). Consequently, the field is grappling with controversies surrounding several crucial concepts, including the existence, coding principles, and mechanisms of dopaminergic transmission modes that might connect the diverse firing patterns of dopaminergic neurons to various behaviors.

In this study, we developed an approach that combines imaging with genetically encoded GPCR-activation-based-dopamine ($GRAB_{DA}$) sensors and fast-scan cyclic voltammetry (FSCV). This method, coupled with a genetically encoded sensor–based image analysis program (GESIAP) (*17*), enabled us to concurrently observe dopaminergic transmission at various sites surrounding the release, including synaptic, perisynaptic, proximate, and distal extrasynaptic locations. Our findings revealed that the diverse firing patterns of dopaminergic neurons give rise to different transmission modes. These transmission modes encode information about the firing frequency, pulse number, and synchrony, incorporating the neurotransmitter quantity, releasing synapse count, and involvement of synaptic or volume transmission. Specifically, quantities of released dopamine exhibit a logarithmic relationship with stimulation frequencies. Moreover, quantities of dopamine-releasing synapses show a linear correlation with numbers of synchronously activated axons. In addition, the counts of dopamine-releasing synapses convey some information from pulse numbers at low stimulation frequencies but not at high stimulation frequencies. Last, during tonic and low-frequency phasic activities, transporters efficiently reuptake dopamine at perisynaptic sites. This confines dopamine within synaptic clefts, thereby mediating synaptic transmission modes. Conversely, during high-frequency activities, especially when synchronized or when transporter function is inhibited, released dopamine could overwhelm transporters. As a result, excess dopamine escapes synaptic clefts through one, two, or occasionally three exit channels, potentially initiating volume-based transmission modes. The findings reveal that dopaminergic neurons use the versatile repertoire of firing modes to exert precise control over dopamine release and diffusion. These data suggest that the coordinated interplay among channeled synaptic enclosures, synaptic properties, and DATs is instrumental in orchestrating a diverse spectrum of transmission modes and determining the coding principles of dopaminergic transmission modes.

RESULTS

Multiplexed GRAB-based imaging and FSCV recordings

We conducted a comprehensive investigation into synaptic, perisynaptic, proximate, and distal extrasynaptic dopaminergic transmission. Our approach involved a multiplex strategy that integrated

[1]Department of Pharmacology, University of Virginia School of Medicine, Charlottesville, VA 22903, USA. [2]Department of Chemistry, University of Virginia, Charlottesville, VA 22904, USA. [3]Department of Psychiatry, University of Virginia School of Medicine, Charlottesville, VA 22903, USA.
*Corresponding author. Email: jventon@virginia.edu

genetically encoded sensor–based functional imaging with FSCV in an ex vivo preparation of the mouse nucleus accumbens (Fig. 1A). Specifically, we initiated the experiments by introducing Sindbis viral expression of $GRAB_{DA}$ (see Materials and Methods for the selection of dopamine sensor) (*18*), in the nucleus accumbens in vivo. Approximately 18 hours after expression, we prepared acute brain accumbal slices and used a local stimulating electrode to activate incoming dopaminergic fibers. We made simultaneous recordings of the evoked fluorescence responses of $GRAB_{DA}$-expressing neurons with widefield epifluorescence imaging and voltammetric responses with a Dagan ChemClamp potentiostat and a T-650 carbon-fiber microelectrode (CFME) positioned adjacent to $GRAB_{DA}$-expressing neurons (Fig. 1B). The electrochemical detection of dopamine used a triangular waveform with a holding potential of −0.4 V and a switching potential at 1.3 V at a rate of 400 V/s, which is delivered to the CFME by the potentiostat (*12*, *19*).

One pressing question in the field pertains to how dopamine participates into broad functions and whether it may use multiple transmission modes to facilitate distinct behavioral actions (*1*–*3*). To address this query, we applied electric stimulations mimicking low-frequency tonic firing at ~2 Hz, short bursts of five spikes at ~8 Hz, and short bursts of eight spikes at ~25 and ~32 Hz (Fig. 1, C to E), which are associated with behaviors during wakefulness, alertness or response to punishment, small to medium rewards, and

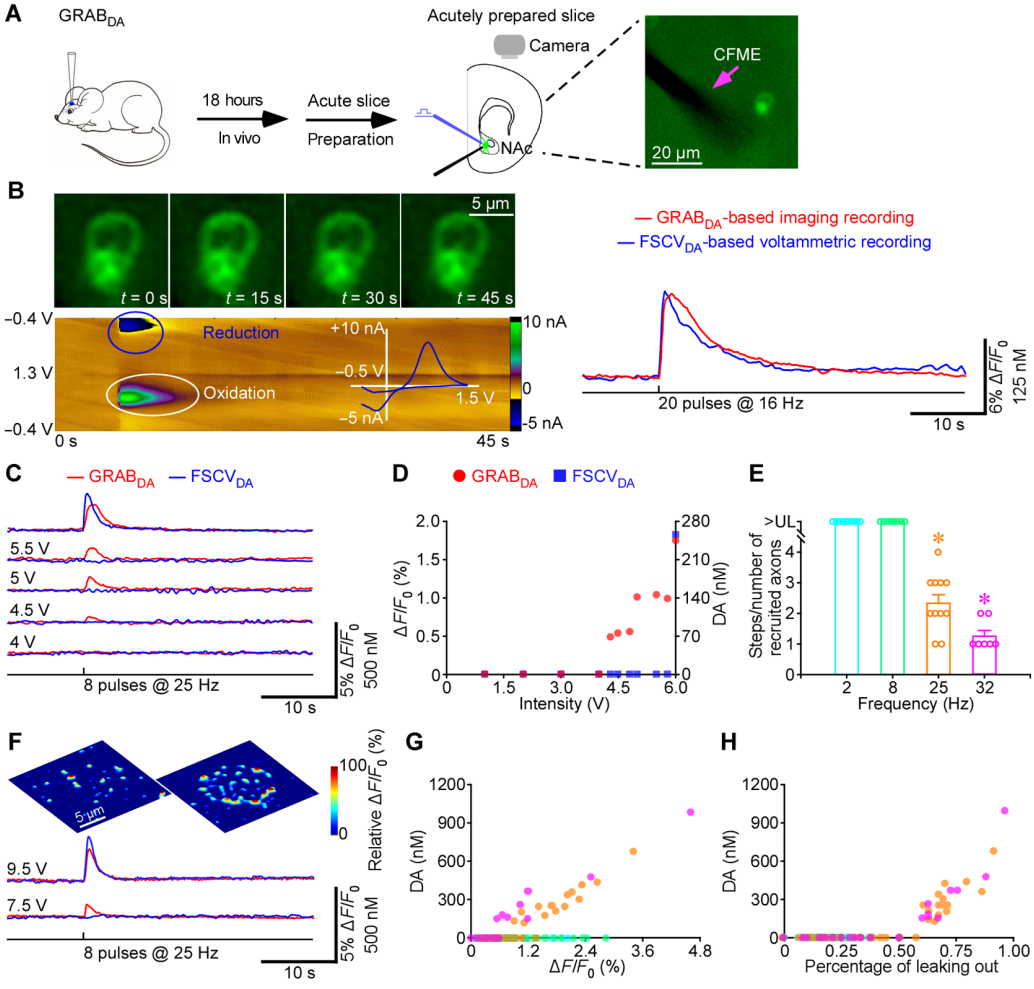

Fig. 1. Multiplexed $GRAB_{DA}$- and $FSCV_{DA}$-based recordings reveal multiple dopaminergic transmission modes. (**A**) Schematic of multiplexed imaging and voltammetry in a mouse nucleus accumbal (NAc) slice preparation. Note the CFME, indicated by a pink arrow, positioned near an expressing accumbal neuron (right image). (**B**) Snapshots of fluorescence $\Delta F/F_0$ responses (top left), a color plot of cyclic voltammogram (bottom left), and concurrent $\Delta F/F_0$ and voltammetric recordings of evoked dopamine (DA) release (right). (**C**) $GRAB_{DA}$ and $FSCV_{DA}$ recordings in response to 8-pulse 25-Hz stimuli delivered at varied intensities. Note the stepwise increase in whole-cell average $\Delta F/F_0$ responses, suggesting the recruitment of more axons with elevated stimulus intensity. (**D**) Maximal whole-cell average $\Delta F/F_0$ responses and dopamine concentrations measured with $GRAB_{DA}$ (red circle) and $FSCV_{DA}$ (blue square) in response to the stimuli. (**E**) $GRAB_{DA}$ response steps/number of recruited axons required to trigger $FSCV_{DA}$ signals under various stimuli (20 pulses at 2 Hz, >top limit; 8 pulses at 8 Hz, >top limit; 8 pulses at 25 Hz, 2.36 ± 0.28; 8 pulses at 32 Hz, 1.29 ± 0.18). The steps/number of recruited axons required for 8 pulses at 25 Hz ($P < 0.001$ and $U = 0.00$) and 32 Hz ($P < 0.001$ and $U = 70.00$) were significantly smaller than those for 20 pulses at 2 Hz. Asterisks indicate $P < 0.05$ ($n = 7$ to 11 neurons from five animals, rank sum nonparametric tests). (**F**) Heatmaps of evoked $\Delta F/F_0$ responses and $GRAB_{DA}$ and $FSCV_{DA}$ recordings in response to 8-pulse 25-Hz stimuli delivered at voltages of 7.5 and 9.5 V. (**G** and **H**) Plot of voltammetric responses against whole-cell average $\Delta F/F_0$ responses (G) and percentages of individual releasing synapses (H), with an expanded dopamine diffusion profile in response to the various stimuli. Note the occurrence of voltammetric responses corresponding to a minimum of 65% $\Delta F/F_0$ and 60% individual releasing synapses, with an expanded dopamine diffusion profile.

large rewards or salient stimuli, respectively (*7*–*10*). We found that stimulations of short bursts of eight spikes at 25 and 32 Hz resulted in varied responses, which appeared to be contingent on intensity (Fig. 1, C to E). To examine whether responses depend on the recruitment of more presynaptic axons as electric stimulation intensity increases, we applied a minimal stimulation protocol. Figure 1 (C and D) shows that low-intensity stimuli (1.0, 2.0, 3.0, and 4.0 V) of eight pulses at 25 Hz evoked neither $GRAB_{DA}$ fluorescence nor $FSCV_{DA}$ voltammetric responses. Higher-intensity stimuli (4.3, 4.5, and 4.7 V) elicited small, consistent $GRAB_{DA}$ fluorescence responses but no $FSCV_{DA}$ responses. Even higher-intensity stimuli (5.0, 5.5, and 5.8 V) doubled the size of $GRAB_{DA}$ fluorescence responses, still without $FSCV_{DA}$ responses. Only the highest-intensity stimuli (6.0 V) elicited both triple-sized $GRAB_{DA}$ fluorescence responses and $FSCV_{DA}$ voltammetric responses. Similar response patterns were found for stimuli consisting of eight pulses at 32 Hz (Fig. 1E). These results suggest that simultaneous activation of multiple dopaminergic axons or neuronal pools, as observed in certain dopamine-related behaviors (*7*, *9*), elicits both $GRAB_{DA}$ fluorescence and $FSCV_{DA}$ voltammetric responses. This dual response, involving the detection of dopamine at extracellular space by $FSCV_{DA}$, indicates the dispersion of dopamine beyond individual $GRAB_{DA}$-expressing neurons and the activation of volume transmission. On the other hand, stimulations of tonic firing at 2 Hz and brief bursts of five spikes at 8 Hz, across varied intensities, exclusively triggered $GRAB_{DA}$ fluorescence responses without detectable $FSCV_{DA}$ voltammetric responses (Fig. 1E). The low levels of extracellular dopamine signals, which were below the $FSCV_{DA}$ detection level of ~2 nM and insufficient to support meaningful extrasynaptic dopaminergic transmission (*11*), suggest restricted transmission.

We made additional analysis of the $GRAB_{DA}$ fluorescence responses with a GESIAP, which allows visualization of dopamine diffusion at individual releasing synapses (*17*). GESIAP unveiled a clear correlation between extracellular $FSCV_{DA}$ responses and heightened $GRAB_{DA}$ fluorescence responses, specifically in conjunction with expanded dopamine diffusion at these releasing synapses (Fig. 1F). Our observations indicated that volume transmission was associated with a minimum of ~0.65% $\Delta F/F_0$ whole-cell average $GRAB_{DA}$ fluorescence responses and at least ~60% of individual releasing synapses exhibiting an expanded dopamine diffusion profile (Fig. 1, G and H).

Transporters control dopamine diffusion without affecting release

Earlier studies propose that DATs play a key role in the regulation of dopamine diffusion postrelease (*11*, *12*). To explore the exact regulatory mechanisms, we investigated the impact of cocaine, a potent inhibitor of DATs (*20*), on simultaneously recorded $GRAB_{DA}$ fluorescence and $FSCV_{DA}$ voltammetric responses in the ex vivo mouse accumbal preparation. Bath application of cocaine extended the time course of both $GRAB_{DA}$ fluorescence and $FSCV_{DA}$ voltammetric responses. While cocaine enhanced the amplitude of $FSCV_{DA}$ voltammetric responses at extracellular sites, it did not alter the magnitude of fluorescence responses at $GRAB_{DA}$-expressing neurons (Fig. 2, A to E). The results imply that cocaine may augment extracellular dopaminergic transmission by inhibiting dopamine reuptake without increasing its release.

The lack of a noticeable effect on the amplitude of evoked $GRAB_{DA}$ fluorescence responses due to transporter inhibition contradicts an earlier proposition, speculating that this inhibition, which is known to enhance extracellular dopaminergic transmission, might trigger increased dopamine release (*13*, *14*). To explore whether cocaine affects dopamine release, we used GESIAP to directly assess dopaminergic transmission properties. Cocaine application lengthened the decay time course of evoked fluorescence $GRAB_{DA}$ responses but did not alter the number of releasing synapses at $GRAB_{DA}$-expressing accumbal neurons, as visualized with GESIAP (Fig. 3, A to C, and movie S1). Electric pulse trains at 0.1 Hz evoked fluorescence $\Delta F/F_0$ responses, manifesting as stochastic failures and release events at single releasing synapses on both the soma and dendrite of $GRAB_{DA}$-expressing neurons (Fig. 3D and fig. S1, A and B). The quantal events at both locations had identical rise times and decay time constants (Fig. 3, D to F, and fig. S1, B to D). Analyzing $\Delta F/F_0$ amplitude histograms of quantal events, adapted from classic quantal analysis methods (*21*), revealed multiple nearly equally spaced peaks (Fig. 3G). The quantal analysis yielded the same synaptic properties for releasing synapses on the soma and dendrite (Fig. 3, G to J, and fig. S1, E to G). On average, there were ~1.1 vesicular quanta, with occasional events of up to two to three vesicular quanta per stimulus, a vesicular quantal size of ~2.2% $\Delta F/F_0$ for dopamine, and a release probability P_r of ~0.65 to 0.70 (release success rate over multiple trials) at single releasing synapses. We calibrated the dopamine concentration–fluorescence response curve for $GRAB_{DA}$ (fig. S2), suggesting that the transmitter released from single vesicles generated ~100 nM dopamine at individual releasing synapses on the soma and dendrite. These results likely underestimate the true concentration but suggest that dopaminergic releasing synapses on the soma and dendrite share the same synaptic properties.

We next found that applying a bath solution containing tetrodotoxin (TTX) or high Mg^{2+}, which blocks synaptic transmission (*22*), eliminated the quantal release events (figs. S3 and S4), confirming

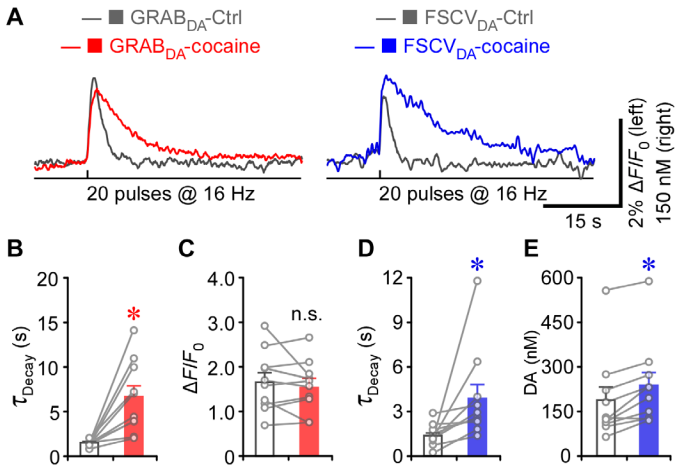

Fig. 2. Dopamine transporter inhibition enhances dopamine signals. (**A**) Simultaneous $GRAB_{DA}$ and $FSCV_{DA}$ recordings of evoked $GRAB_{DA}$ fluorescence $\Delta F/F_0$ and $FSCV_{DA}$ voltammetric responses in the nucleus accumbens before (gray) and after (red and blue) the bath application of 3-μm cocaine. (**B** and **C**) Peak amplitudes [Control (Ctrl), 1.68 ± 0.21%; cocaine, 1.57 ± 0.18%; $Z = -0.80$, $P = 0.47$] and decay time constants (Ctrl, 1.65 ± 0.09 s; cocaine, 6.70 ± 1.27 s; $Z = 2.85$, $P = 0.002$) of $\Delta F/F_0$ responses before (gray) and after (red) cocaine application. (**D** and **E**) Peak amplitudes (Ctrl, 192.4 ± 45.2 nM; cocaine, 240.0 ± 44.1 nM; $Z = 2.70$, $P = 0.004$) and decay time constants (Ctrl, 1.43 ± 0.23 s; cocaine, 3.89 ± 0.97 s; $Z = 2.80$, $P = 0.002$) of voltammetric responses before (gray) and after (blue) cocaine application. *$P < 0.05$ ($n = 10$ neurons from six animals, Wilcoxon tests). n.s., not significant.

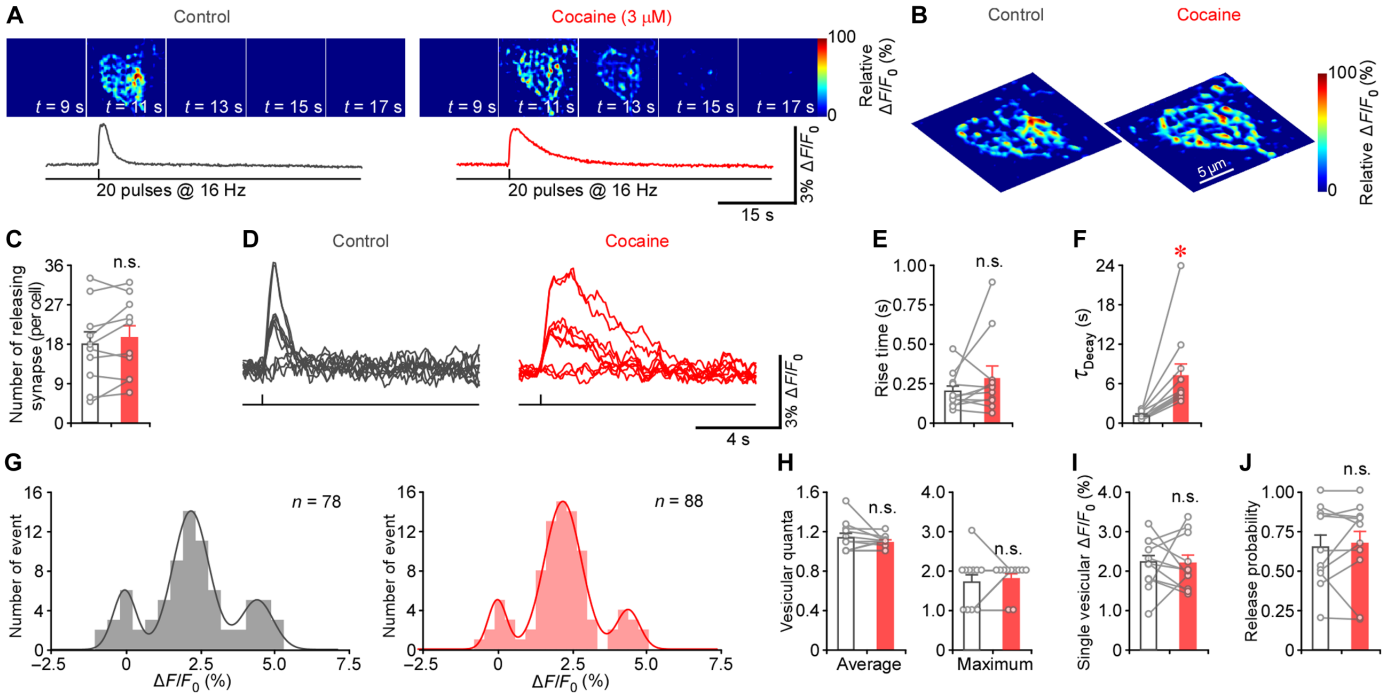

Fig. 3. Transporter inhibition elongates dopamine signals without changing release properties. (**A**) Heatmaps of electrically evoked fluorescence $\Delta F/F_0$ responses in the nucleus accumbens before (left) and after (right) bath application of 3 μM cocaine. (**B**) Three-dimensional (3D) spatiotemporal profiling of $\Delta F/F_0$ responses before (left) and after (right) cocaine application. Scale bar applies to all in (B). (**C**) Releasing synapse counts before (gray) and after (red) bath application of cocaine (Ctrl, 17.70 ± 2.91; cocaine, 19.40 ± 2.84; $Z = 1.38$, $P = 0.19$). (**D**) Ten $\Delta F/F_0$ responses evoked by single pulse stimuli at isolated releasing synapses before (gray) and after (red) bath application of cocaine. (**E** and **F**) Ten to ninety percent rise times (Ctrl, 0.20 ± 0.03 s; cocaine, 0.28 ± 0.07 s; $Z = 0.93$, $P = 0.37$) and decay time constants (Ctrl, 1.16 ± 0.21 s; cocaine, 7.32 ± 1.81 s; $Z = 2.93$, $P < 0.001$) of $\Delta F/F_0$ responses before (gray) and after (red) cocaine application. (**G**) Amplitude histograms of $\Delta F/F_0$ responses before (gray) and after (red) bath application of cocaine. (**H** to **J**) Average (Ctrl, 1.14 ± 0.05; cocaine: 1.10 ± 0.02; $Z = 0.43$, $P = 0.43$) and maximal (Ctrl, 1.73 ± 0.20; cocaine, 1.82 ± 0.12; $Z = 0.58$, $P = 0.75$) vesicular quanta, quantal sizes (Ctrl, 2.21 ± 0.19%; cocaine, 2.20 ± 0.20%; $Z = -0.27$, $P = 0.83$), and release probabilities (Ctrl, 65.18 ± 7.52%; cocaine, 67.40 ± 8.05%; $Z = 0.36$, $P = 0.77$) before (gray) and after (red) cocaine application. *$P < 0.05$ ($n = 10$ to 11 neurons from six animals, Wilcoxon tests).

their synaptic origin (*23*, *24*). Moreover, TTX application revealed the low occurrence of TTX-insensitive quantal events (zero events per 5 to 10 min, $n = 10$ neurons from six animals). These results indicate a high dependence of dopamine release on action potentials, which is consistent with a previous report (*25*). As a control, we measured the time course of quantal events using a different dopamine sensor, dLight, which has ~10 times faster kinetics (*26*). This sensor showed identical rise times and decay time constants (fig. S5). These results suggest that both $GRAB_{DA}$ and dLight can track the dynamics of synaptically released dopamine. Analysis of cocaine's effects revealed that the transporter inhibitor did not alter the rise time of quantal release events but did enhance the decay time constant of quantal responses (Fig. 3, D to F). Cocaine application did not change any of the other synaptic properties, including quantal size, quantal content, and release probability (Fig. 3, G to J). These results confirm that cocaine prolongs dopaminergic signals by inhibiting reuptake and extending the decay time of responses without affecting dopamine release properties.

To assess the generalizability of these findings, we investigated the impact of cocaine on dopamine diffusion in an ex vivo prefrontal cortical preparation. The application of cocaine in the bath solution resulted in a prolonged decay time course of evoked fluorescence responses at $GRAB_{DA}$-expressing cortical neurons, while the response amplitude remained unaffected (Fig. 4, A to D). Likewise, no noticeable alteration occurred in the number of releasing synapses at $GRAB_{DA}$-expressing cortical neurons (Fig. 4, E and F). Moreover, cocaine induced no change in the rise time of quantal release events but notably extended the decay time constant of these responses (Fig. 4, G and H). Quantal analysis revealed consistent numbers of released vesicles, almost invariably ~1.0 vesicular quanta and very occasionally up to two vesicular quanta per stimulus before and after cocaine application (Fig. 4, I and J). Furthermore, this analysis disclosed the same vesicular quantal size of ~2.0% $\Delta F/F_0$ of dopamine at single releasing synapses, and the release probability remained unchanged, maintaining a value of ~0.55 at single releasing synapses before and after cocaine application (Fig. 4K). Together, these results suggest that the cocaine-induced inhibition of transporters elongates dopaminergic signals without directly affecting the release of dopamine itself.

To further corroborate our findings, we used GBR 12935, a selective DAT inhibitor (*20*), in the mouse ex vivo accumbal preparation. GBR 12935 prolonged the decay time course of evoked fluorescence $GRAB_{DA}$ responses without changing the number of releasing synapses at $GRAB_{DA}$-expressing accumbal neurons (fig. S6, A to C). Again, GBR 12935 did not alter the rise time of quantal release events but notably extended the decay time constant of these responses (fig. S6, D to F). Quantal analysis revealed the same numbers of released vesicles, averaging ~1.1 vesicular quanta and occasionally up to two to three vesicular quanta per stimulus before and after GBR 12935 application (fig. S6, G and H). This analysis

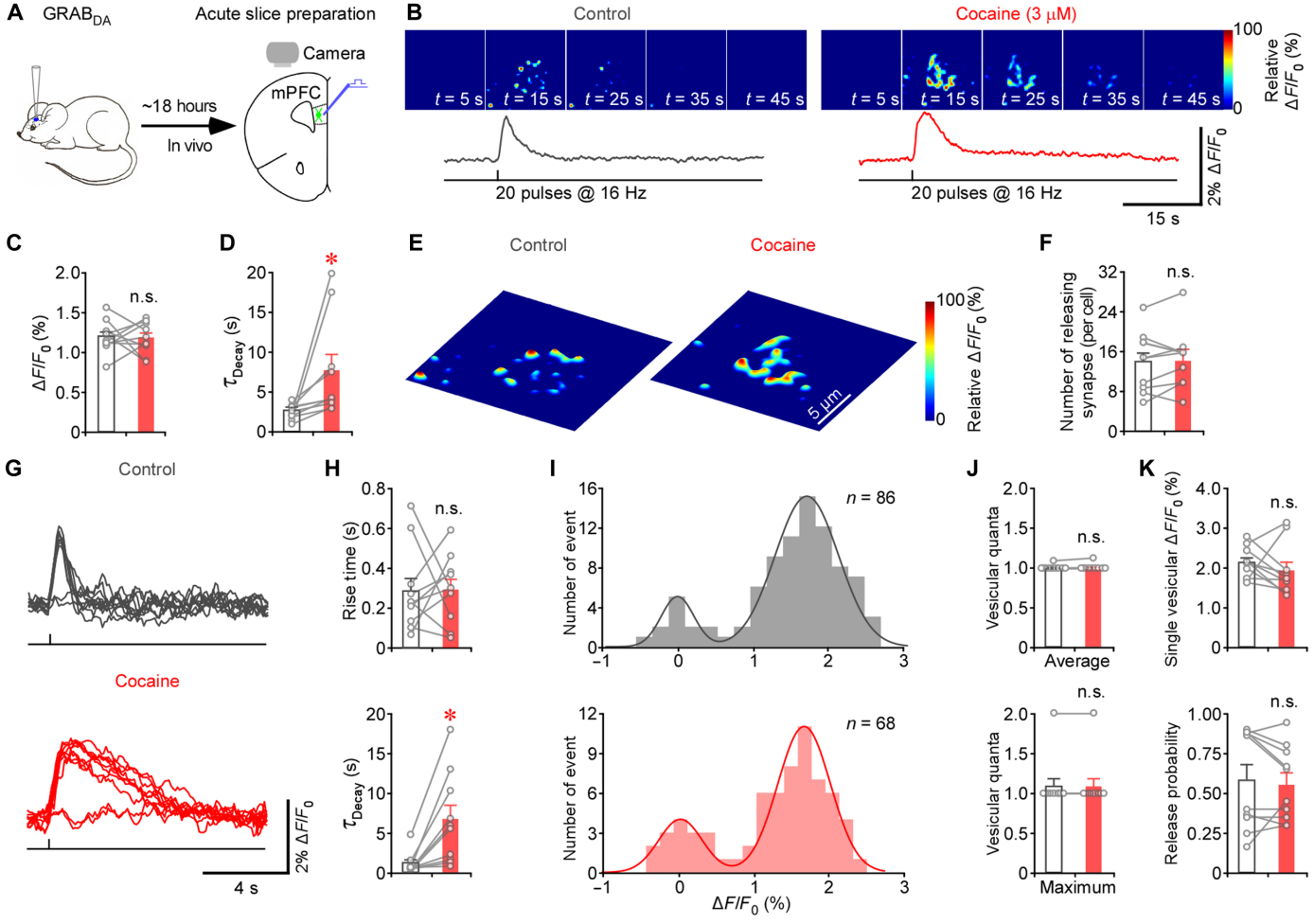

Fig. 4. Transporter inhibition elongates dopamine signals without altering release properties in the mouse prefrontal cortex. (**A**) Schematic of experimental design in an mPFC slice preparation. (**B**) Heatmaps of electrically evoked fluorescence $\Delta F/F_0$ responses before (left) and after (right) bath application of 3 μM cocaine. Color scale bar applies to all in (B). (**C** and **D**) Amplitudes (Ctrl, 1.19 ± 0.06%; cocaine, 1.17 ± 0.06%; $Z = -0.15$, $P = 0.92$) and decay time constants (Ctrl, 2.68 ± 0.29 s; cocaine, 7.68 ± 1.96 s; $Z = 2.80$, $P = 0.002$) of $\Delta F/F_0$ responses before (gray) and after (red) cocaine application. (**E**) 3D spatiotemporal profiling of $\Delta F/F_0$ responses before (left) and after (right) cocaine application. (**F**) Releasing synapse counts before (gray) and after (red) cocaine application (Ctrl, 14.30 ± 1.89; cocaine, 14.80 ± 1.86; $Z = -0.15$, $P = 0.92$). (**G**) Ten $\Delta F/F_0$ responses evoked by single pulse stimuli at isolated releasing synapses before (gray) and after (red) cocaine application. (**H**) Ten to ninety percent rise times (Ctrl, 0.29 ± 0.07 s; cocaine: 0.30 ± 0.05 s; $Z = 0.06$, $P = 1.0$) and decay time constants (Ctrl, 1.19 ± 0.42 s; cocaine, 6.60 ± 1.78 s; $Z = 2.80$, $P = 0.002$) of $\Delta F/F_0$ responses before (gray) and after (red) cocaine application. (**I**) Amplitude histograms of $\Delta F/F_0$ responses before (gray) and after (red) bath application of cocaine. (**J** and **K**) Average (Ctrl, 1.01 ± 0.01; cocaine, 1.01 ± 0.01; $Z = 1.00$, $P = 1.00$) and maximal (Ctrl, 1.10 ± 0.1; cocaine, 1.10 ± 0.10; $Z = 0.00$, $P = 1.00$) vesicular quanta, quantal sizes (Ctrl, 2.13 ± 0.12%; cocaine, 1.93 ± 0.20%; $Z = -1.27$, $P = 0.23$), and release probabilities (Ctrl, 59.18 ± 9.72%; cocaine, 56.14 ± 7.28%; $Z = -0.98$, $P = 0.38$) before (gray) and after (red) cocaine application. *$P < 0.05$ ($n = 10$ neurons from five animals, Wilcoxon tests).

also confirmed a consistent vesicular quantal size of ~1.5% $\Delta F/F_0$ dopamine and an unaltered release probability of ~0.65 at single releasing synapses before and after GBR 12935 application (fig. S6, I and J). Collectively, these findings consistently support the notion that transporter inhibition prolongs dopaminergic signals without affecting dopamine release.

Transporters gate dopamine diffusion at perisynaptic sites

To understand how transporters influence dopamine dispersion, we used GESIAP to visualize dopamine diffusion at synaptic, perisynaptic, and extrasynaptic areas before and after bath application of cocaine (Fig. 5A). GESIAP created the dopamine spatial diffusion profiles with pixel-wise maximal $\Delta F/F_0$ plots, revealing that under normal conditions, dopamine diffusion at those well-isolated releasing synapses fit well with a single-exponential decay function that yielded a dopamine spread length constant of ~0.60 μm at accumbal neurons (Fig. 5, B and C). In the presence of cocaine, pixel-wise maximal $\Delta F/F_0$ plots floated upward at ~0.5 μm away from the releasing synapses (Fig. 5, B and C). Arbitrarily fitting the plots with a single-exponential decay function gave an estimation of a larger dopamine spread length constant of ~0.80 μm at accumbal neurons (Fig. 5C), indicating a substantial effect of cocaine on the spatial diffusion of released dopamine.

Using GESIAP, we generated high-resolution profiles of dopamine spatial diffusion at well-isolated releasing synapses. In the control condition, dopamine concentration rapidly decreased as it diffused away from the release center. The diffusion pattern usually took the shape of a circular cone. Measurements of the full width at half maximum (FWHM) for minor and major axes were alike,

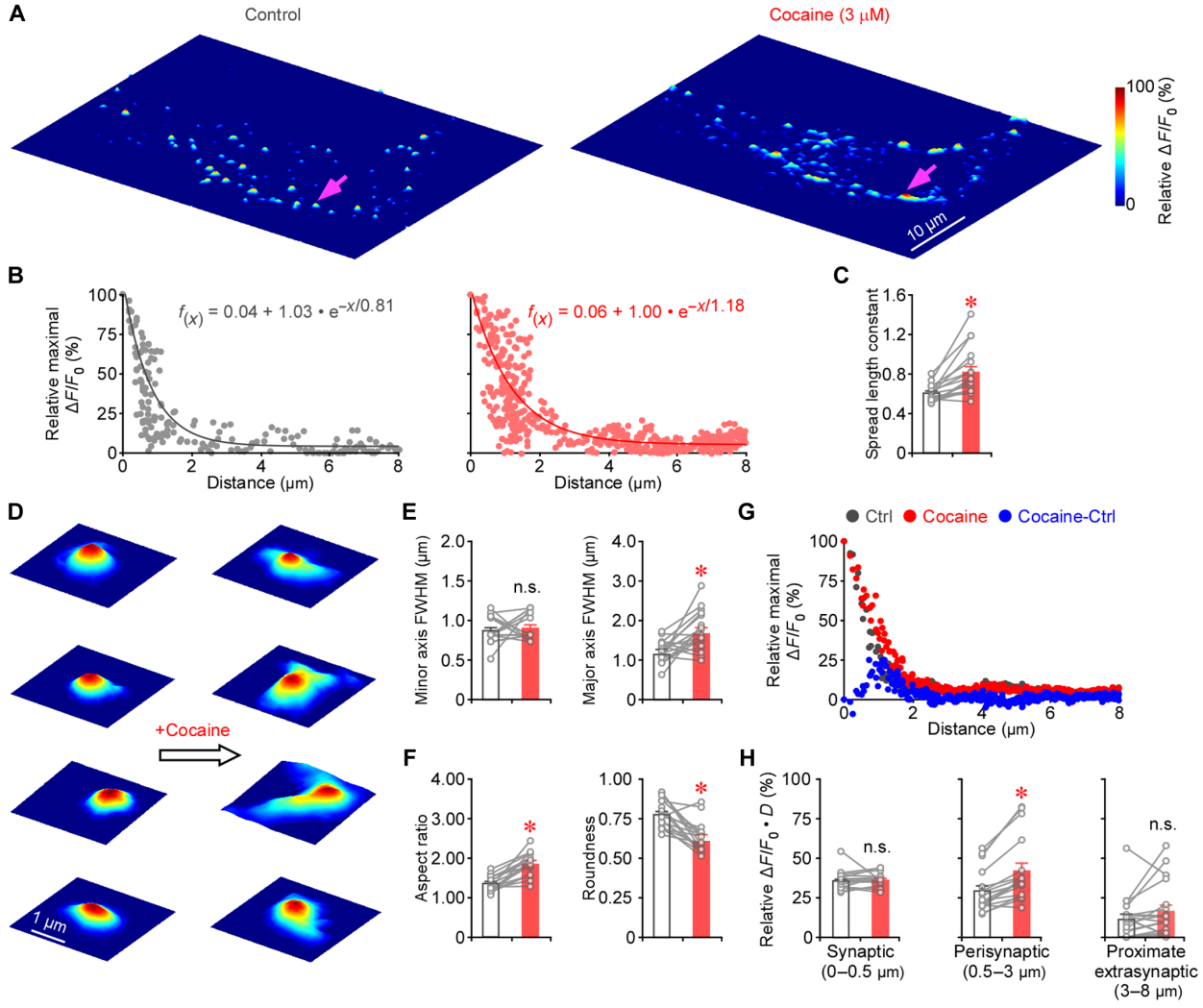

Fig. 5. Transporter inhibition drives extrasynaptic diffusion of dopamine. (**A**) 3D spatiotemporal profiling of electrically evoked fluorescence $\Delta F/F_0$ responses in the nucleus accumbens before (left) and after (right) the bath application of 3 μM cocaine. (**B**) Pixel-wise maximal $\Delta F/F_0$ plots before (left) and after (right) cocaine application at the same isolated releasing synapse indicated by the pink arrows in (A). (**C**) Averaged spatial spread length constants (Ctrl, 0.60 ± 0.02 μm; cocaine, 0.81 ± 0.06 μm; $Z = 3.68$, $P < 0.001$). (**D**) 3D profiling of $\Delta F/F_0$ responses at isolated releasing synapses before and after cocaine application. Note the dopamine leaking out of synapses via 1 to 3 (average, 1.67 ± 0.16) exit channels after cocaine application. Scale bar applies to all in (D). (**E**) Minor (Ctrl, 0.87 ± 0.04 μm; cocaine, 0.90 ± 0.04 μm; $Z = 0.37$, $P = 0.72$) and major (Ctrl, 1.20 ± 0.06 μm; cocaine, 1.70 ± 0.12 μm; $Z = 2.94$, $P = 0.002$) FWHMs of dopamine diffusion profiles at isolated releasing synapses before and after cocaine application. (**F**) Aspect ratios (Ctrl, 1.37 ± 0.05; cocaine, 1.86 ± 0.07; $Z = 3.72$, $P < 0.001$) and roundness (Ctrl, 0.77 ± 0.02; cocaine, 0.63 ± 0.02; $Z = -3.50$, $P < 0.001$) values of dopamine diffusion profiles at isolated releasing synapses before and after cocaine application. (**G**) Plots of pixel-wise maximal $\Delta F/F_0$ before (gray) and after (red) cocaine application and their difference (blue; cocaine-Ctrl). (**H**) Relative integration values of $\Delta F/F_0$ at distances of 0.5 μm (Ctrl, 0.36 ± 0.01; cocaine, 0.36 ± 0.01; $Z = 1.22$, $P = 0.23$), 0.5 to 3 μm (Ctrl, 0.30 ± 0.03; cocaine, 0.42 ± 0.05; $Z = 3.68$, $P < 0.001$), and 3 to 8 μm (Ctrl, 0.12 ± 0.03; cocaine, 0.17 ± 0.04; $Z = 1.81$, $P = 0.07$). *$P < 0.05$ ($n = 18$ neurons from 6 animals, Wilcoxon tests).

falling within the range of ~0.9 to 1.2 μm (Fig. 5, D and E, and movie S2). Cocaine expanded the diffusion profiles, exposing one to three exit channels through which dopamine traveled ~1 to 5 μm to disperse into the extracellular space. This transformation shifted the profile from a circular to an elliptical cone shape. Specifically, while the minor axis' FWHM remained consistent at ~0.9 μm, the major axis' FWHM expanded to ~1.7 μm (Fig. 5, D to F, and movie S2). Quantitative analysis of the diffusion profiles revealed that while cocaine had little effect on dopamine accumulation and diffusion within a radius of ~0.5 μm from the release center, it enhanced dopamine accumulation, slowed its diffusion between the radii of ~0.5 to 3 μm from the release center, and slightly increased dopamine buildup beyond the radius of ~3 μm from the release center (Fig. 5, G and H). These results indicate the primary effect site of cocaine to be ~0.5 to 3 μm from the release center, the perisynaptic area where DATs are highly expressed (*27*–*29*).

In our prefrontal cortical preparation, we confirmed the impact of transporters on dopamine diffusion. Once more, cocaine was observed to broaden the dopamine diffusion at $GRAB_{DA}$-expressing cortical neurons (Fig. 6, A to C). This alteration transformed the diffusion profile from a circular cone–like shape to an elliptical cone–like form, revealing one to three egress channels through which

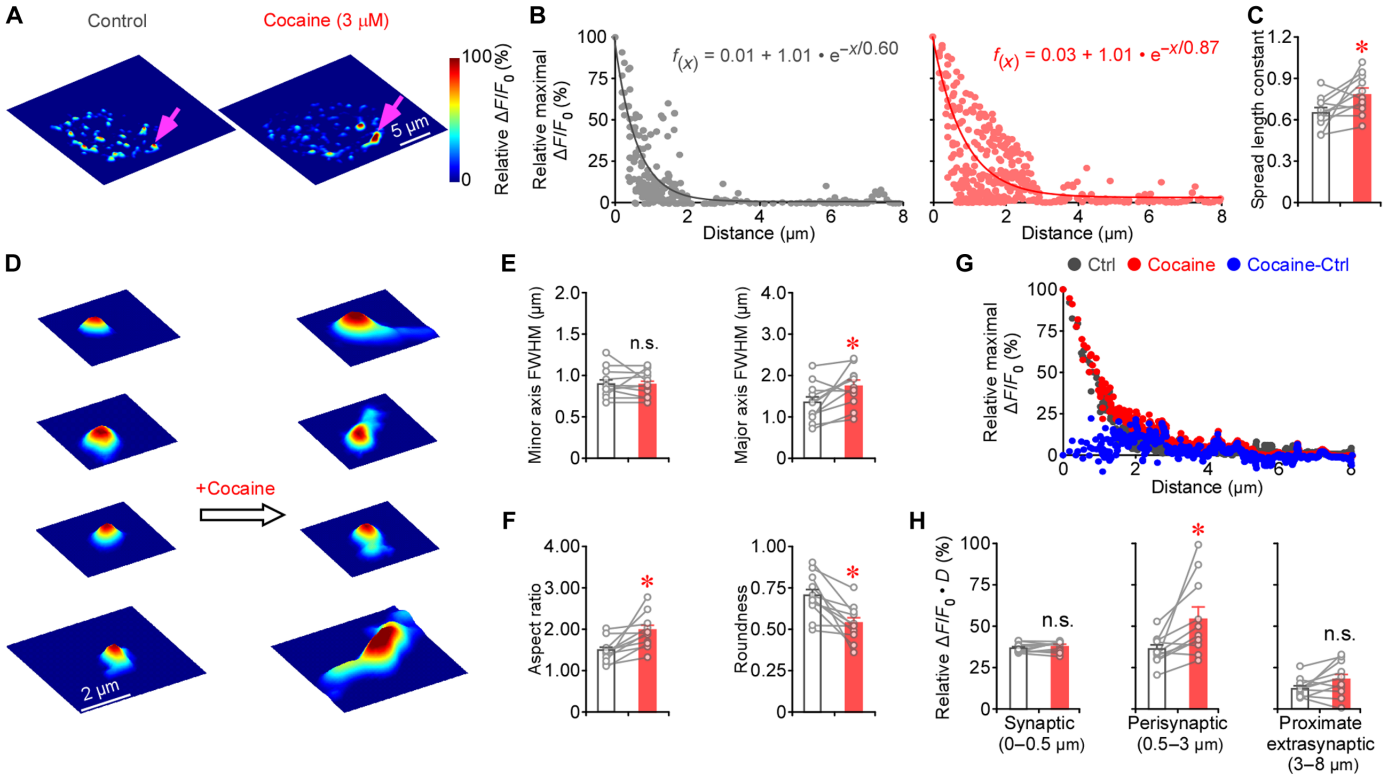

Fig. 6. Transporter inhibition drives extrasynaptic diffusion of dopamine in mPFC. (**A**) 3D spatiotemporal profiling of electrically evoked fluorescence $\Delta F/F_0$ responses in the prefrontal cortex before (left) and after (right) the bath application of 3-μm cocaine. (**B**) Pixel-wise maximal $\Delta F/F_0$ plots before (left) and after (right) cocaine application at the same isolated releasing synapse indicated by the pink arrows in (A). (**C**) Averaged spatial spread length constants (Ctrl, 0.65 ± 0.03 μm; cocaine, 0.78 ± 0.04 μm; $Z = 2.19$, $P = 0.027$). (**D**) 3D profiling of $\Delta F/F_0$ responses at isolated releasing synapses before and after cocaine application. Note the dopamine leaking out of the synapses via 1 to 3 (average, 1.55 ± 0.21) exit channels after cocaine application. Scale bar applies to all in (D). (**E**) Minor (Ctrl, 0.90 ± 0.05 μm; cocaine, 0.89 ± 0.05 μm; $Z = -0.56$, $P = 0.64$) and major (Ctrl, 1.35 ± 0.14 μm; cocaine, 1.73 ± 0.14 μm; $Z = 2.40$, $P = 0.014$) FWHMs of dopamine diffusion profiles at isolated releasing synapses before and after cocaine application. (**F**) Aspect ratios (Ctrl, 1.47 ± 0.09; cocaine, 1.95 ± 0.12; $Z = 2.93$, $P < 0.001$) and roundnesses (Ctrl, 0.70 ± 0.04; cocaine, 0.53 ± 0.03; $Z = -2.93$, $P < 0.001$) of dopamine diffusion profiles at isolated releasing synapses before and after cocaine application. (**G**) Plots of pixel-wise maximal $\Delta F/F_0$ before (gray) and after (red) cocaine application and their difference (blue; cocaine-Ctrl). (**H**) Relative integration values of $\Delta F/F_0$ at distances of 0.5 μm (Ctrl, 0.36 ± 0.01; cocaine, 0.37 ± 0.01; $Z = 1.16$, $P = 0.28$), 0.5 to 3 μm (Ctrl, 0.35 ± 0.03; cocaine, 0.54 ± 0.07; $Z = 2.67$, $P = 0.005$), and 3 to 8 μm (Ctrl, 0.13 ± 0.02; cocaine, 0.18 ± 0.03; $Z = 1.87$, $P = 0.067$). *$P < 0.05$ ($n = 11$ neurons from five animals, Wilcoxon tests).

dopamine traveled ~1 to 5 μm to reach the extracellular space (Fig. 6, D to F). Specifically, cocaine exhibited minimal effect on dopamine accumulation and diffusion within a radius of ~0.5 μm from the release center. However, it notably intensified dopamine accumulation and slowed its diffusion between radii of ~0.5 and 3 μm from the release center. Furthermore, it marginally increased dopamine buildup at distances of ~3 μm or more from the release center (Fig. 6, G and H). Together, these results illustrate the general impact of cocaine on dopamine diffusion after its release.

We further verified the findings with the selective DAT inhibitor GBR 12935 in the mouse accumbal preparation. Similarly, GBR expanded dopamine diffusion at $GRAB_{DA}$-expressing accumbal neurons, altering the diffusion profile from a circular cone–like to an elliptical cone–like shape. This transformation revealed one to three pathways through which dopamine traveled ~1 to 5 μm before spreading into the extracellular space (fig. S7, A to F). Once again, GBR had minimal impact on dopamine accumulation and diffusion within a radius of ~0.5 μm from the release center, increased dopamine accumulation, slowed its diffusion between radii of ~0.5 and 3 μm from the release center, and marginally elevated dopamine buildup at distances of ~3 μm or more from the release center (fig. S7, G and H).

To rule out the possibility of nonspecific involvement by other neurotransmitters, we conducted two sets of control experiments using the accumbal preparation. Bath application of inhibitors targeting nicotine receptors (-Rs), AMPA-Rs, *N*-methyl-D-aspartate (NMDA)–Rs, γ-aminobutyric acid type A ($GABA_A$)–Rs, and $GABA_B$-Rs, using Dihydro-β-erythroidine hydrobromide (DHβE), 2,3-dioxo-6-nitro-7-sulfamoylbenzo[*f*]quinoxaline (NBQX), D-(-)-2-Amino-5-phosphonopentanoic acid (AP5), Picrotoxin (PTX), and CGP 55845, respectively, showed no influence on the dopamine diffusion profile (fig. S8). In addition, to achieve more selective dopamine release, we adapted an all-optical approach. Specifically, we used in vivo adeno-associated virus (AAV) viral expression of Cre-dependent ChrimsonR-tdTomato in dopaminergic neurons in the ventral tegmental area, followed by Sindbis viral expression of $GRAB_{DA}$ in accumbal neurons of DAT-Cre mice, in which Cre recombinase expression is governed by the *DAT* promoter (fig. S9A). Subsequently, in the acute slice preparation, we used optogenetic activation of dopaminergic fibers to induce dopamine release. Cocaine induced the same transformation in the diffusion pattern

of dopamine released via optogenetic stimulation (fig. S9 and movie S3). Collectively, these findings support the general role of DATs in regulating dopamine diffusion after its release.

Dopaminergic transmission modes encode the properties of firing modes

The preceding data highlighted the considerable influence of dopamine release and its interplay with transporters in dopamine signaling. Subsequently, our investigation centered on systematically exploring how distinct modes of dopaminergic transmission encode the specific characteristics of various firing modes within dopaminergic neurons (Fig. 7). We found that as stimulation frequency increased, the evoked fluorescence $\Delta F/F_0$ responses escalated (Fig. 7A and movie S4). Plotting $\Delta F/F_0$ responses against stimulation frequencies showed a more pronounced increase at lower-frequency ranges, and converting the *x* axis into logarithmical scale revealed a logarithmic relationship between $\Delta F/F_0$ responses and stimulation frequencies (Fig. 7B). Moreover, the number of dopamine-releasing synapses showed a direct correlation with the number of synchronously activated axons (Fig. 7, C and D, and movie S5), revealing an additional dimension of the coding mechanism. Last, the number of dopamine-releasing synapses exhibited a positive correlation with pulse numbers at low stimulation frequencies, but not at high frequencies (Fig. 7, C and D), representing a third facet of the coding scheme. Notably, the number of dopamine-releasing synapses was largely independent of stimulation frequencies. These findings, alongside the analysis of synaptic and volume transmission, illuminate that dopamine uses neurotransmitter quantity and releasing synapse count to encode the frequency, number, and synchronicity of firing pulses while using additional volume transmission to signal heightened firing activities.

DISCUSSION

In this study, we multiplexed genetically encoded sensor–based functional imaging with FSCV and further integrated the method with the super-resolution imaging analysis program GESIAP. The approach allowed us to monitor dopaminergic transmission simultaneously at synaptic, perisynaptic, proximate, and distal extrasynaptic sites. We found how various firing patterns of dopaminergic neurons lead to distinct transmission modes, unveiling the coding principles behind this transformation. Specifically, dopaminergic transmission encodes information on the frequency, number, and synchrony of firing pulses by incorporating the neurotransmitter quantity, count of releasing synapses, and involvement of synaptic and/or volume transmission. Our findings underscore the precise cooperation between channeled synaptic enclosures, synaptic properties, and transporters in orchestrating this spectrum of transmission modes.

Coding of diverse firing patterns

Dopaminergic neurons display diverse firing patterns associated with various behaviors such as wakefulness, alertness, responses to punishment, reactions to rewards of different magnitudes, and salient stimuli (*7*–*10*). The long-standing question is whether varied firing modes of dopaminergic neurons facilitate the generation of distinct dopamine signals, thereby contributing to specific modulations in various behaviors and diseases (*1*–*3*). However, obtaining a definitive answer to this query has proven to be more challenging than anticipated because of limitations in current dopamine monitoring techniques. Here, we introduce an approach enabling high-resolution visualization of individual releasing synapses at dopaminergic synapses. Our analysis illustrates that dopaminergic neurons encode the frequency, number, and synchrony of their firing pulses with the amount of dopamine released and the number of releasing synapses. Notably, high-frequency and synchronized firing overwhelms DATs, resulting in dopamine being dispersed into the extracellular space and triggering volume transmission. By adjusting transmitter quantity, releasing synapse count, and using synaptic and/or volume transmission, dopaminergic neurons effectively transform diverse firing modes into distinct intercellular signals. The complexity of these signals has the potential to convey heterogeneous firing patterns to varied spatiotemporally defined G protein–coupled receptor signaling in postsynaptic targets, initiating a range of functions (*4*, *30*, *31*).

Regulation of synaptic diffusion of dopamine

This study illustrates how dopamine diffusion is precisely regulated at synapses, which initiates controlled synaptic and/or volume transmission in accordance with behavior-associated firing patterns. These findings align with our previous imaging studies of neuromodulators and neuropeptides (*17*, *24*, *32*), challenging the prevailing theory that neuromodulators, including dopamine, primarily rely on volume transmission. The volume transmission theory posits that neuromodulatory transmitters diffuse widely, influencing a number of nearby cells (*33*, *34*). However, this theory hinges largely on the assumption that endogenously released neuromodulators behave akin to exogenously applied ones that freely diffuse in the extrasynaptic space—an assumption yet to be supported by direct experimental evidence (*35*, *36*). Voltammetric experiments, typically detecting only extracellular signals, are inadequate for validating this model (*11*, *12*). A few patch-clamp studies ingeniously used mathematical models to simulate evoked neuromodulatory releases, estimating dopamine spread areas to be ~2 to 30 μm in diameter (*15*, *16*). However, these studies were somewhat overlooked, possibly because of their reliance on indirect calculation methods or assumptions within the simulations.

In this study, simultaneous nanoscopic imaging of dopamine at synaptic, perisynaptic, and extrasynaptic sites offers a direct method to visualize released dopamine diffusion and understand its regulatory properties. Overall, released dopamine molecules form as a circular cone–shaped diffusion pattern. At synaptic sites, within a radius of ~0.2 to 0.5 μm from the release center, dopamine molecules appear to diffuse freely and rapidly, reaching a high, relatively uniform concentration of dopamine after the release. These image-defined releasing synapses closely match the anatomical size of dopaminergic synapses, measured at ~0.65 to 0.75 μm in diameter under electron microscopes (*37*–*39*). However, at perisynaptic and nearby extrasynaptic sites, most dopamine molecules are swiftly intercepted by DATs, resulting in a rapid decrease in dopamine concentration and often leaving only a negligible fraction to escape synapses, which is frequently undetectable by FSCV. These extrasynaptic sites are where DATs are highly expressed (*27*–*29*). During heightened activity–induced release or transporter inhibition, a slightly larger amount of dopamine molecules manages to escape out of synapses through one, two, or occasionally three exit channels. Despite this increase, the quantity typically remains below the sensor-based imaging detection threshold yet becomes discernible by FSCV at distal extrasynaptic sites. This corresponds to low

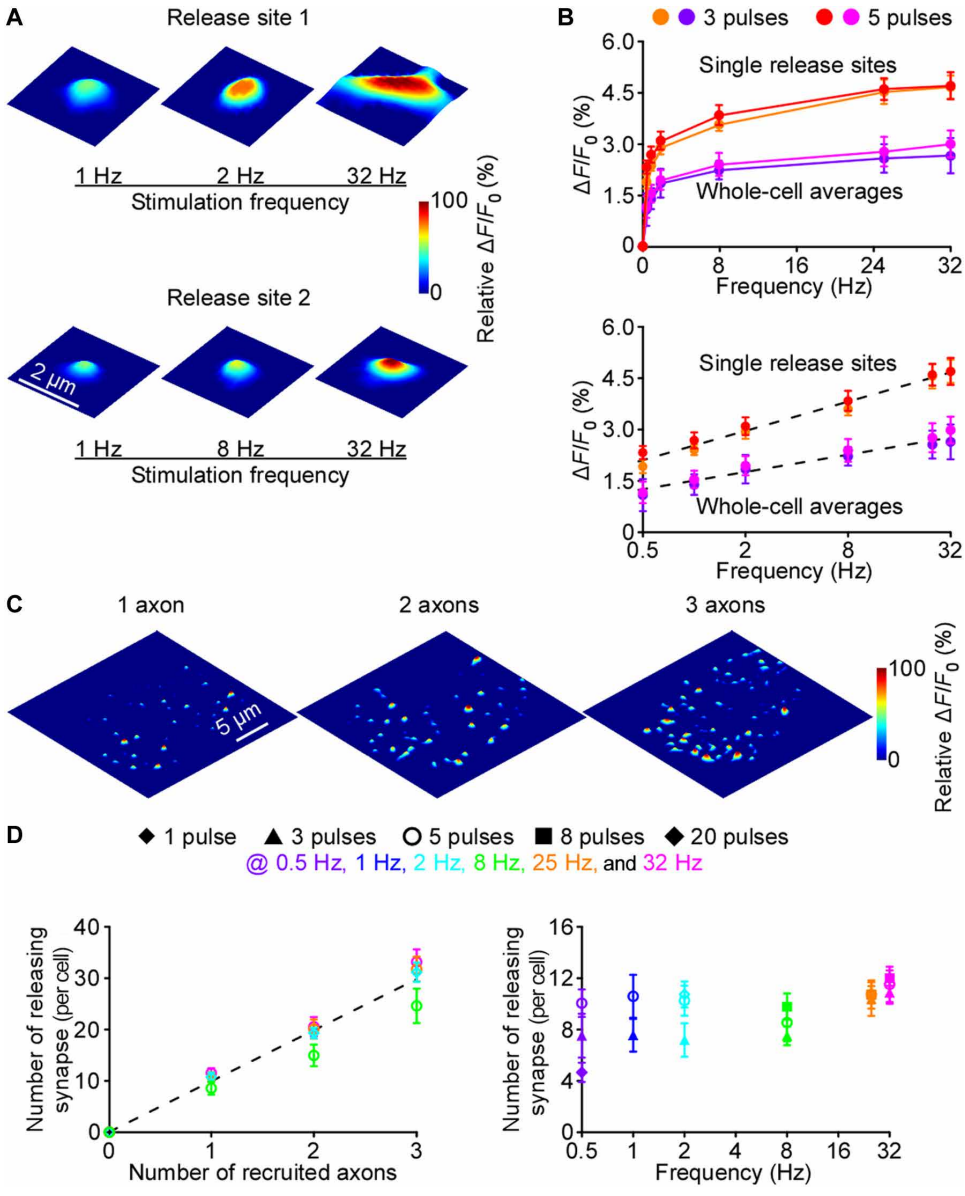

Fig. 7. Dopamine release properties encode frequency, number, and synchrony of firing pulses. (**A**) Heatmaps of fluorescence $\Delta F/F_0$ responses evoked by five-pulse stimuli at two releasing synapses in the nucleus accumbens. (**B**) Top: Plot of whole-cell average and single releasing synapse maximal $\Delta F/F_0$ responses against frequencies of three-pulse [whole-cell, 0.5 Hz (1.06 ± 0.47%), 1 Hz (1.38 ± 0.30%), 2 Hz (1.83 ± 0.41%), 8 Hz (2.20 ± 0.27%), 25 Hz (2.54 ± 0.41%), and 32 Hz (2.63 ± 0.51%); synapse, 0.5 Hz (1.87 ± 0.19%), 1 Hz (2.35 ± 0.14%), 2 Hz (2.87 ± 0.20%), 8 Hz (3.53 ± 0.19%), 25 Hz (4.48 ± 0.35%), and 32 Hz (4.62 ± 0.34%)] and five-pulse [whole-cell, 0.5 Hz (1.13 ± 0.31%), 1 Hz (1.51 ± 0.25%), 2 Hz (1.90 ± 0.25%), 8 Hz (2.35 ± 0.33%), 25 Hz (2.72 ± 0.42%), and 32 Hz (2.94 ± 0.39%); synapse, 0.5 Hz (2.88 ± 0.19%), 1 Hz (2.64 ± 0.23%), 2 Hz (3.05 ± 0.26%), 8 Hz (3.78 ± 0.29%), 25 Hz (4.54 ± 0.31%), and 32 Hz (4.63 ± 0.39%)] stimuli (n = 6 to 10 cells or 18 to 26 synapses from four to five animals). Bottom: Plot of $\Delta F/F_0$ responses against logarithmic stimulation frequencies. Note that the correlations fitted with log functions $f_{(x)} = 1.45 + 0.27 \cdot \log(x)$ ($r = 0.99$, $F = 263.89$, and $P < 0.001$) and $f_{(x)} = 2.50 + 0.42 \cdot \log(x)$ ($r = 1.00$, $F = 1393.97$, and $P < 0.001$). (**C**) Heatmaps of elevated $\Delta F/F_0$ responses evoked by eight-pulse stimuli with increased intensities that recruit presumably one, two, or three axons. (**D**) Left: Plot correlating the number of releasing synapses with presumably recruited axons. Note that the correlation fitted with a linear function of $f_{(x)} = 0.01 + 9.85 \cdot x$ ($r = 0.99$, $F = 623.38$, and $P < 0.001$). Right: Plot of the number of releasing synapses against steps 1 to 3 $\Delta F/F_0$ responses in response to the stimuli delivered at 0.5 Hz (1 pulse, 4.60 ± 0.75; 3 pulses, 7.50 ± 1.85; 5 pulses, 9.83 ± 1.06), 1 Hz (3 pulses, 7.50 ± 1.26; 5 pulses, 10.33 ± 1.76), 2 Hz (3 pulses, 7.14 ± 1.28; 5 pulses, 10.00 ± 1.15; 20 pulses, 10.67 ± 0.98), 8 Hz (3 pulses, 7.50 ± 0.76; 5 pulses, 8.50 ± 1.24; 8 pulses, 9.78 ± 1.12), 25 Hz (3 pulses, 10.20 ± 1.27; 5 pulses, 10.80 ± 0.94; 8 pulses, 10.86 ± 0.69), and 32 Hz (3 pulses, 10.67 ± 0.87; 5 pulses, 11.56 ± 0.94; 8 pulses, 11.87 ± 0.58) (n = 6 to 21 neurons from four to five animals).

dopamine concentrations of ~1 to 10 nM at these distal extrasynaptic sites, which may activate high-affinity receptors, such as D3 receptors (*40*), potentially initiating functional volume transmission (*11*).

Our finding suggests the presence of a physical barrier or channeled synaptic enclosure that confines dopamine within synapses. While this discovery challenges the perception of neuromodulatory synaptic clefts as fairly open cellular spaces, it aligns with ultrastructural observations of abundant curve-shaped astrocytic gap junctions forming annular or tapered annular profiles, with widths of ~0.5 to 2 μm and lengths of up to ~6 to 10 μm at putative dopaminergic perisynaptic sites (*41*). The organized structure of channeled synaptic enclosures seems to significantly facilitate and possibly direct the efficient dispersion of dopamine into extracellular sites, thereby enabling its crucial role in mediating volume transmission. In the future, directly colocalizing gap junctions and transporters at dopamine-releasing synapses with ultrastructural reconstruction after imaging experiments would provide more compelling evidence to support this model. In addition, owing to the spatial resolution limitations of $FSCV_{DA}$, it remains to be determined whether dopamine diffuses freely or through specific channels that are physically restricted by cellular structures and/or regulated by transporters at the distal extracellular space.

On the basis of the dopamine concentration–fluorescence response curve obtained from our perfusion experiments and the previous study (*18*), we estimated that ~50 to 100 nM dopamine is released per quantal event. At these concentrations, fewer than one dopamine molecule would be present in the cleft volume of dopaminergic synapses, which have a diameter of ~0.65 to 0.75 μm (*37*–*39*). This seems implausible. Previous studies suggest that D2 receptors may exhibit much lower affinity at synapses—by a factor of ~50 to 500 times (*42*–*45*). Given that synaptic $GRAB_{DA}$ sensors share similar pharmacological properties with D2 receptors (*46*), their synaptic affinity might also be substantially lower. As a result, synaptic dopamine concentrations may have been underestimated by a similar factor, implying that ~2.5 to 50 mM dopamine could be released per quantal event, consistent with the findings from two previous reports (*26*, *45*). This apparent discrepancy might stem from limited access of exogenous dopamine to synaptic clefts due to structural constraints. To resolve this, it is critical to directly measure the synaptically evoked dopamine concentration–fluorescence response relationship, as previously demonstrated by Patriarchi *et al*. (*26*) and Marcott *et al*. (*45*). Such an experiment would provide accurate calibration of the dopamine concentration released per quantal event and validate the main conclusions of this study.

Biological and clinical implication

Intercellular communication, which is mediated by fast-acting transmitters glutamate and GABA and by hundreds (>500) of slow-acting neuromodulatory transmitters (e.g., monoamines, neuropeptides, and other molecules), orchestrates diverse behavioral and physiological processes (*47*, *48*). Much knowledge has been gained through the remarkable sensitivity and temporal resolution of electrophysiological recordings and herculean experiments focused on fast glutamatergic and GABAergic transmission (*49*–*51*). In particular, in the early 1990s, the advent of high-resolution patch-clamp recordings enabled the quantitative analysis of glutamatergic and GABAergic synaptic transmissions and their properties (*52*–*54*). The technique catalyzed a wave of discoveries concerning synaptic transmission and plasticity. These breakthroughs encompassed silent synapses, synaptic receptor trafficking, synaptic molecular signaling, synaptic nanoscale organization, and many other vital insights crucial for comprehending the brain, body, and associated disorders and, ultimately, for identifying pathogenic mechanisms and therapeutic strategies (*48*, *55*–*57*). Unfortunately, patch-clamp recordings are crippled by minimal and/or desensitizing neuromodulator-induced electrophysiological responses (*58*). Alternative methods, such as microdialysis and voltammetry, despite many recent improvements, lack necessary spatial and/or temporal resolution (*59*, *60*). Therefore, despite years of research that implicates numerous slow-acting neuromodulatory transmitters in a myriad of physiological actions and diseases, there remains a dearth of quantitative and mechanistic insights into neuromodulatory regulation and function. The emergence of genetically encoded fluorescence sensors, many of which emit abundant photons, presents a promising avenue. Our theoretical groundwork suggests that using image analysis algorithms could convert surplus collected photons into improved spatial and temporal resolutions, potentially decoding transmission in healthy and diseased brains (*32*, *61*).

Our recently developed image analysis algorithms facilitate the delineation of fundamental properties—such as the extent of transmitter spatial diffusion, quantal size, quantal content, release probability, pool size, and refilling rate—at individual releasing synapses across different cell types (neurons, astrocytes, and other nonneuronal cells) in various animal species (mouse, rat, and human) for various transmitters (*17*, *24*). Here, we demonstrate nanoscopic visualization of dopamine release and diffusion across distinct behavior-related activity patterns. These visualizations reveal the collaborative role of channeled synaptic enclosures, synaptic properties, and transporters in shaping dopaminergic transmission modes. This mechanism explains why cocaine may elevate extracellular dopamine levels, as observed in voltammetry (*13*, *14*), without affecting dopamine release at synapses. Notably, much like DATs (*62*–*64*), channeled synaptic enclosures and synaptic properties may change under both physiological and pathological conditions (*32*, *65*, *66*). Therefore, these findings predicate that synaptic enclosures, properties, and transporters all have the capacity to affect behaviors and contribute to the development of diseases. Moreover, this study establishes a methodology to quantify how synaptic enclosures, properties, and transporters affect transmission mechanisms governing a wide array of dopamine-related behaviors, including sleep and wake cycles, alertness, attention, reward and motivation, movement and motor control, and learning and memory (*1*–*4*). This advancement should aid in deciphering synaptic mechanisms implicated in a wide spectrum of diseases, such as attention-deficit/hyperactivity disorder, bipolar disorder, Parkinson's disease, major depressive disorders, substance use disorders, and schizophrenia (*2*–*4*, *67*).

MATERIALS ANS METHODS

Animal preparations

C57BL/6J mice (the Jackson Laboratory, Bar Harbor, ME; RRID: IMSR_JAX:000664), along with the DAT-Cre mice (the Jackson Laboratory; RRID: IMSR_JAX:006660) bred congenically on the C57BL/6J background, were used in this study. Genotyping was conducted through standard polymerase chain reaction using genomic DNA extracted from tail samples using Cre primers (5′-TGG CTG TTG GTG TAA AGT GG-3′ and 5′-CCA AAA GAC GGC AAT ATG GT-3′) and internal positive control primers (5′-TGG

CTG TTG GTG TAA AGT GG-3′ and 5′-GGA CAG GGA CAT GGT TGA CT-3′). Heterozygous DAT-Cre mice exhibiting specific DNA bands at both the Cre and internal positive control positions were included in the experiments.

Both male and female postnatal animals, aged 42 to 60 days, were included, and neither genetically encoded sensor–based imaging nor FSCV detected any difference in dopaminergic responses measured in tissues prepared from males versus females. Animals were maintained in the animal facility at the University of Virginia and family housed or pair housed in the temperature-controlled animal room with a 12/12-hour light/dark cycle. Food and water were available ad libitum. All procedures for animal and human cell line experiments were performed following protocols (no. 3168) approved by the Animal Care & Use Committee of the University of Virginia and in accordance with US National Institutes of Health guidelines.

Viral preparation and expression

Genetically encoded fluorescent sensors for dopamine, $GRAB_{DA2m}$ (*18*), $GRAB_{DA3m}$ (*68*), and dLight (*26*), were subcloned into Sindbis viral vector pSinREP5 with Xba I and Sph I restriction digestion, and viral particles were produced and expressed following our previous studies (*17*, *23*, *69*). After preliminary testing of the dopamine sensors $GRAB_{DA2m}$, $GRAB_{DA3m}$, and dLight, we selected $GRAB_{DA2m}$ as the preferred sensor for our experiments. This preference was due to $GRAB_{DA2m}$'s dynamic range, which encompasses the full spectrum of dopamine concentration changes at individual releasing synapses and cells, effectively translating these variations into varying fluorescence responses without saturation (fig. S2) (*18*). In addition, its higher baseline fluorescence made it easier to identify expressing cells. For in vivo sensor expression, animals were initially anesthetized by an intraperitoneal injection of ketamine and xylazine (10 and 2 mg/kg, respectively) and then placed in a stereotaxic frame. A glass pipette was used to penetrate the dorsal nucleus accumbens, the prelimbic cortex, and/or the ventral tegmental area according to stereotaxic coordinates to deliver ~50 nl of Sindbis or AAV solution by pressure injection to infect neurons. Experiments were typically performed within 18 ± 4 hours of Sindbis viral infection.

For the in vivo expression of these constructs, animals were initially anesthetized via intraperitoneal injection of ketamine and xylazine at doses of 10 and 2 mg/kg, respectively. Subsequently, they were securely positioned within a stereotaxic frame. A 0.5-mm-diameter drill bit was used to create a craniotomy above the designated injection sites, and viral solutions were administered into various brain regions based on their specific stereotaxic coordinates using a pulled glass micropipette and pressure injection. In imaging experiments, 100 nl of Sindbis $GRAB_{DA}$ viral solution was delivered in the medial nucleus accumbens (anterior-posterior (AP): −1.35 mm; medial-lateral (ML): 0.75 mm; dorsal-ventral (DV), −4.30 mm), or the deep layers of the prelimbic cortex (AP, 1.97 mm; ML, 0.50 mm; DV, −2.50 mm), both of which are heavily innovated by dopaminergic fibers (*70*, *71*). For optogenetic experiments, 80 nl of AAV-Syn-FLEX-ChrimsonR-tdTomato viral solution (Addgene, Watertown, MA; RRID: Addgene_62723) was injected into the ventral tegmental area (AP, −3.20 mm; ML, 0.50 mm; DV, −4.50 mm) (*70*). The injection micropipette was typically left in the brain for ~10 min after the injection to ensure proper viral diffusion. Experiments were typically conducted within 18 ± 4 hours after Sindbis viral infection and 5 to 6 weeks after AAV viral infection to achieve optimal expression (*72*, *73*).

Acute brain slice preparation

The preparation of acute nucleus accumbal and frontal cortical slices followed the procedures outlined in our previous reports (*17*, *69*). Briefly, animals were deeply anesthetized by xylazine-ketamine and decapitated. The brain containing the nucleus accumbens or frontal cortex was swiftly removed and immersed in cold (0° to 4°C) oxygenated physiological solution containing 125 mM NaCl, 2.5 mM KCl, 1.25 mM NaH_2PO_4, 25 mM $NaHCO_3$, 1 mM $MgCl_2$, 25 mM dextrose, and 2 mM $CaCl_2$ (pH 7.4). Coronal slices (400 μm thick) were cut from the brain blocks. These slices were equilibrated in oxygenated physiological solution at a temperature of 37.0° ± 0.5°C for ~0.5 to 1 hour before sensor imaging and FSCV recordings.

During imaging and FSCV recordings, the brain slices were submerged in a chamber and stabilized with a fine nylon net attached to a platinum ring. The recording chamber was perfused with oxygenated physiological solution. The half-time for the bath solution exchange was ~6 s, and the temperature of the bath solution was maintained at 34.0° ± 0.5°C. All antagonists were bath applied.

Electric and optogenetic activation of dopamine release

Dopamine release was induced either through electrical or optogenetic means. For precise control over local stimulation to incrementally recruit individual axons, we used a bipolar cluster stimulating electrode (CE2C65, FHC, Bowdoin, ME). Electric pulses lasting 1 ms, with intensities varying from 4 to 10 V, were administered. To minimize interference between dopamine and other neurotransmitters, particularly acetylcholine (*74*, *75*), we positioned the stimulating electrode adjacent to the nucleus accumbens and the prelimbic cortex, targeting incoming dopaminergic fibers. The approach seemed effective as we observed no acetylcholine-dependent depression in dopamine signals following repetitive stimulations (Fig. 2) (*74*). Moreover, dopamine signals remained unaffected after the bath application of DHβE, NBQX, AP5, PTX, and CGP targeting nicotine receptors (-Rs), AMPA-Rs, NMDA-Rs, $GABA_A$-Rs, and $GABA_B$-Rs, respectively (fig. S8). Furthermore, optogenetic activation of dopaminergic fibers yielded consistent results (fig. S9).

For optogenetic manipulation of dopamine release, a 200-μm-diameter optical fiber (Thorlabs, Newton, NJ) was positioned near the nucleus accumbens along the dopaminergic fiber pathway to activate ChrimsonR using a 635-nm laser (Opto Engine LLC, Midvale, UT). The optogenetic stimulation used single 20-ms light pulses, with the light intensity set to 10 mW/mm^2 at the fiber tip. In addition, 0.6 mM tetraethylammonium was introduced into the bath solution to facilitate optogenetic activation. To prevent unintended opsin activation during the simultaneous $GRAB_{DA}$ sensor–based imaging, a low sensor excitation light intensity of 0.07 mW/mm^2 was typically used in these experiments. Moreover, given the substantial power needed for optogenetic activation and to ensure no interference of the optogenetic excitation light with $GRAB_{DA}$ fluorescence responses, two to three frames of images obtained during optogenetic stimulation were omitted before analysis.

Calibration of genetically encoded sensor $GRAB_{DA}$

Calibration of $GRAB_{DA}$ fluorescence responses was performed using the ex vivo nucleus accumbens slice preparation. Dopamine solutions (catalog no. 3548, Tocris Bioscience, Minneapolis, MN) at varying concentrations were perfused onto single $GRAB_{DA}$-expressing accumbal neurons. A glass patch pipette with a ~4-μm

tip was filled with dopamine solution and mounted on a Luigs-Neumann JUNIOR COMPACT manipulator. The pipette was then rapidly positioned at ~50 μm from a $GRAB_{DA}$-expressing neuron, aimed directly at it (*72*). Dopamine solution was expelled from the pipette using a constant air pressure of ~50 Pa.

Genetically encoded sensor–based imaging

Because of the slow nature of neuromodulatory transmission, long-term imaging (from seconds to minutes) became necessary to capture the action of transmitters and resolve their properties. To minimize drift and fluctuation vital for high-resolution visualization of transmitter release–induced fluorescence responses (*32*, *61*), a stable recording/stimulation and imaging setup was used to carry out all imaging and FSCV recording experiments (*76*, *77*). Widefield epifluorescence imaging was performed using a Hamamatsu ORCA FLASH4.0 camera (Hamamatsu Photonics, Shizuka, Japan), and fluorescent sensor–expressing cells in acutely prepared tissue slices were excited by a 460-nm ultrahigh-power low-noise light-emitting diode (Prizmatix, Givat-Shmuel, Israel) (*69*, *76*). The light intensity was typically set at 0.20 mW/mm^2, unless stated otherwise. The frame rate of the FLASH4.0 camera was set to 10 to 50 Hz. Fluorescence signals were collected with an Olympus 40× water immersion objective with a numerical aperture of 0.8. Despite the variable fluorescence F_0 across the entire cell membrane surface of expressing neurons due to heterogeneous $GRAB_{DA}$ sensor expression, the $\Delta F/F_0$ responses showed no or weak correlation with the basal fluorescence F_0, suggesting independence from sensor expression levels and reliability in measuring transmitter concentration (fig. S10) (*17*, *24*).

Imaging analysis with GESIAP

Recent advancements in computational algorithms technology have spurred a swift expansion of applications for super-resolution widefield deconvolution microscopy (*78*, *79*), which can achieve ~150- to 200-nm spatial resolution, sufficient to resolving synapses, including dopaminergic synapses sizing ~0.65 to 0.75 μm in diameter (*37*–*39*). We have previously validated its applicability in sensor-based functional imaging, both theoretically (*32*) and experimentally (*24*). The improved GESIAP program proved to be as effective in extracting fluorescence signals from relatively noisy backgrounds recorded with $GRAB_{DA}$ and dLight sensors, overcoming previous extraction limitations (*32*). The algorithms were created using MATLAB 2023a with MATLAB's Image Processing Toolbox (MathWorks, Natick, MA). The fluorescence response traces typically represented the whole-cell average responses of individual neuronal somata of interest, unless stated otherwise (e.g., single releasing synapses on the soma and dendrite). To visualize individual transmitter releasing synapses and estimate postsynaptic transmitter spatial diffusion extent, the maximal electrically evoked maximal $\Delta F/F_0$ responses at individual pixels over time were plotted to create three-dimensional (3D) spatial profiles for individual transmitter–releasing synapses. Pixels with the maximal $\Delta F/F_0$ responses in individual releasing synapses were assumed to be the centers of release. Fluorescence $\Delta F/F_0$ intensity profiles at well-isolated releasing synapses were fit with a single-exponential decay function, and their decay constants were extracted as the spatial spread length constants. To estimate the quantal properties of individual transmitter releases, 20-pulse trains at low frequency (0.1 Hz) were used to evoked transmitter release, and failures and releases of $\Delta F/F_0$ events at isolated individual releasing synapses were analyzed using a quantal analysis approach (*21*, *52*–*54*), which yielded the vesicle quantal size, quantal content, and release probability.

Fast-scan cyclic voltammetry

Simultaneous FSCV was made with a CFME positioned adjacent to $GRAB_{DA}$-expressing neurons. T-650 CFMEs were fabricated from 7-μm T-650 carbon fibers (Cytec Engineering Materials Inc., Tempe, AZ), which were aspirated into a glass capillary (1.2 mm outer diameter and 0.68 mm inner diameter, A-M System, Sequim, WA) and pulled into electrodes with a PE-22 puller (Narishige International USA Inc., Amityville, NY). The carbon fiber was trimmed to 50 to 100 μm in length from the pulled glass tip. CFMEs were cleaned in isopropyl alcohol for 30 min before detection. For electrochemical detection of dopamine, a triangular waveform was applied with a holding potential at −0.4 V and a switching potential at 1.3 V and at 400 V/s using a Dagan ChemClamp potentiostat (Pine Research Instrumentation, Durham, NC). For data collection and analysis, TarHeel CV (provided by R. M. Wightman, University of North Carolina) was used. For the electrode calibrations, phosphate buffer solution was used, consisting of 131.25 mM NaCl, 3.0 mM KCl, 10.0 mM NaH_2PO_4, 1.2 mM $MgCl_2$, 2.0 mM Na_2SO_4, and 1.2 mM $CaCl_2$ at pH 7.4. A dopamine stock solution was prepared in 0.1 M $HClO_4$ and diluted to 500 nM with phosphate buffer solution for calibrations before the experiment (*19*).

Experimental operation and data collection

The experiments were conducted under control of a single custom-written program based on IGOR (WaveMetrics, Lake Oswego, OR) (*76*, *77*). This program was specifically created for simultaneous operation of electrophysiology, optogenetics, genetically encoded sensor–based functional imaging, and FSCV experiments and for synchronized image capture, electric or optogenetic stimulations, and comprehensive data collection.

Statistical analysis

Statistical results were reported as means ± SEM. Animals or cells were randomly assigned into control or experimental groups, and investigators were blinded to experimental treatments. On the basis of the effect size d calculated from previous and preliminary data, the sample size is estimated to be ≥~8 to 25 per group to attain the desired power of ≥80%, with statistical significance set as $\alpha < 0.05$. Statistical significance of the means is determined using Wilcoxon and Mann-Whitney rank sum nonparametric tests for paired and unpaired samples, respectively. Statistical significance of the relationship of two data groups is determined using regression t test, provided that the normality and constant variance tests are passed.

Supplementary Materials

The PDF file includes:
Figs. S1 to S10

Other Supplementary Material for this manuscript includes the following:
Movies S1 to S5

REFERENCES AND NOTES

1. C. Liu, P. Goel, P. S. Kaeser, Spatial and temporal scales of dopamine transmission. *Nat. Rev. Neurosci.* **22**, 345–358 (2021).
2. T. Sippy, N. X. Tritsch, Unraveling the dynamics of dopamine release and its actions on target cells. *Trends Neurosci.* **46**, 228–239 (2023).

3. J. W. de Jong, K. M. Fraser, S. Lammel, Mesoaccumbal dopamine heterogeneity: What do dopamine firing and release have to do with It? *Annu. Rev. Neurosci.* **45**, 109–129 (2022).
4. S. Zhai, Q. Cui, D. V. Simmons, D. J. Surmeier, Distributed dopaminergic signaling in the basal ganglia and its relationship to motor disability in Parkinson's disease. *Curr. Opin. Neurobiol.* **83**, 102798 (2023).
5. A. A. Grace, B. S. Bunney, The control of firing pattern in nigral dopamine neurons: Burst firing. *J. Neurosci.* **4**, 2877–2890 (1984).
6. K. Otomo, J. Perkins, A. Kulkarni, S. Stojanovic, J. Roeper, C. A. Paladini, In vivo patch-clamp recordings reveal distinct subthreshold signatures and threshold dynamics of midbrain dopamine neurons. *Nat. Commun.* **11**, 6286 (2020).
7. M. Marinelli, J. E. McCutcheon, Heterogeneity of dopamine neuron activity across traits and states. *Neuroscience* **282**, 176–197 (2014).
8. P. D. Dodson, J. K. Dreyer, K. A. Jennings, E. C. Syed, R. Wade-Martins, S. J. Cragg, J. P. Bolam, P. J. Magill, Representation of spontaneous movement by dopaminergic neurons is cell-type selective and disrupted in parkinsonism. *Proc. Natl. Acad. Sci. U.S.A.* **113**, E2180–E2188 (2016).
9. B. I. Hyland, J. N. Reynolds, J. Hay, C. G. Perk, R. Miller, Firing modes of midbrain dopamine cells in the freely moving rat. *Neuroscience* **114**, 475–492 (2002).
10. J. Y. Cohen, S. Haesler, L. Vong, B. B. Lowell, N. Uchida, Neuron-type-specific signals for reward and punishment in the ventral tegmental area. *Nature* **482**, 85–88 (2012).
11. C. A. Owesson-White, M. F. Roitman, L. A. Sombers, A. M. Belle, R. B. Keithley, J. L. Peele, R. M. Carelli, R. M. Wightman, Sources contributing to the average extracellular concentration of dopamine in the nucleus accumbens. *J. Neurochem.* **121**, 252–262 (2012).
12. P. A. Garris, E. L. Ciolkowski, P. Pastore, R. M. Wightman, Efflux of dopamine from the synaptic cleft in the nucleus accumbens of the rat brain. *J. Neurosci.* **14**, 6084–6093 (1994).
13. D. P. Covey, M. F. Roitman, P. A. Garris, Illicit dopamine transients: Reconciling actions of abused drugs. *Trends Neurosci.* **37**, 200–210 (2014).
14. B. J. Venton, A. T. Seipel, P. E. M. Phillips, W. C. Wetsel, D. Gitler, P. Greengard, G. J. Augustine, R. M. Wightman, Cocaine increases dopamine release by mobilization of a synapsin-dependent reserve pool. *J. Neurosci.* **26**, 3206–3209 (2006).
15. N. A. Courtney, C. P. Ford, The timing of dopamine- and noradrenaline-mediated transmission reflects underlying differences in the extent of spillover and pooling. *J. Neurosci.* **34**, 7645–7656 (2014).
16. M. J. Beckstead, D. K. Grandy, K. Wickman, J. T. Williams, Vesicular dopamine release elicits an inhibitory postsynaptic current in midbrain dopamine neurons. *Neuron* **42**, 939–946 (2004).
17. W. S. Zheng, Y. Zhang, R. E. Zhu, P. Zhang, S. Gupta, L. Huang, D. Sahoo, K. Guo, M. E. Glover, K. C. Vadodaria, M. Li, T. Qian, M. Jing, J. Feng, J. Wan, P. M. Borden, F. Ali, A. C. Kwan, L. Gan, L. Lin, F. H. Gage, B. J. Venton, J. S. Marvin, K. Podgorski, S. M. Clinton, M. Zhang, Y. Li, L. L. Looger, J. J. Zhu, GESIAP: A versatile genetically encoded sensor-based image analysis program. bioRxiv 511006 [Preprint] (2022). https://doi.org/10.1101/2022.10.05.511006.
18. F. M. Sun, J. Zhou, B. Dai, T. Qian, J. Zeng, X. Li, Y. Zhuo, Y. Zhang, Y. Wang, C. Qian, K. Tan, J. Feng, H. Dong, D. Lin, G. Cui, Y. Li, Next-generation GRAB sensors for monitoring dopaminergic activity in vivo. *Nat. Methods* **17**, 1156–1166 (2020).
19. E. Privman, B. J. Venton, Comparison of dopamine kinetics in the larval *Drosophila* ventral nerve cord and protocerebrum with improved optogenetic stimulation. *J. Neurochem.* **135**, 695–704 (2015).
20. H. Wang, T. Treadway, D. P. Covey, J. F. Cheer, C. R. Lupica, Cocaine-induced endocannabinoid mobilization in the ventral tegmental area. *Cell Rep.* **12**, 1997–2008 (2015).
21. P. Fatt, B. Katz, Spontaneous subthreshold activity at motor nerve endings. *J. Physiol.* **117**, 109–128 (1952).
22. J. J. Zhu, J. A. Esteban, Y. Hayashi, R. Malinow, Postnatal synaptic potentiation: Delivery of GluR4-containing AMPA receptors by spontaneous activity. *Nat. Neurosci.* **3**, 1098–1106 (2000).
23. J. Wan, W. Peng, X. Li, T. Qian, K. Song, J. Zeng, F. Deng, S. Hao, J. Feng, P. Zhang, Y. Zhang, J. Zou, S. Pan, M. Shin, B. J. Venton, J. J. Zhu, M. Jing, M. Xu, Y. Li, A genetically encoded sensor for measuring serotonin dynamics. *Nat. Neurosci.* **24**, 746–752 (2021).
24. P. K. Zhu, W. S. Zheng, P. Zhang, M. Jing, P. M. Borden, F. Ali, K. Guo, J. Feng, J. S. Marvin, Y. Wang, J. Wan, L. Gan, A. C. Kwan, L. Lin, L. L. Looger, Y. Li, Y. Zhang, Nanoscopic visualization of restricted non-volume cholinergic and monoaminergic transmission with genetically encoded sensors. *Nano Lett.* **20**, 4073–4083 (2020).
25. J. T. Yorgason, D. M. Zeppenfeld, J. T. Williams, Cholinergic interneurons underlie spontaneous dopamine release in nucleus accumbens. *J. Neurosci.* **37**, 2086–2096 (2017).
26. T. Patriarchi, J. R. Cho, K. Merten, M. W. Howe, A. Marley, W.-H. Xiong, R. W. Folk, G. J. Broussard, R. Q. Liang, M. J. Jang, H. N. Zhong, D. Dombeck, M. von Zastrow, A. Nimmerjahn, V. Gradinaru, J. T. Williams, L. Tian, Ultrafast neuronal imaging of dopamine dynamics with designed genetically encoded sensors. *Science* **360**, eaat4422 (2018).
27. D. A. Lewis, D. S. Melchitzky, S. R. Sesack, R. E. Whitehead, S. Auh, A. Sampson, Dopamine transporter immunoreactivity in monkey cerebral cortex: Regional, laminar, and ultrastructural localization. *J. Comp. Neurol.* **432**, 119–136 (2001).
28. S. R. Sesack, V. A. Hawrylak, C. Matus, M. A. Guido, A. I. Levey, Dopamine axon varicosities in the prelimbic division of the rat prefrontal cortex exhibit sparse immunoreactivity for the dopamine transporter. *J. Neurosci.* **18**, 2697–2708 (1998).
29. T. R. Bagalkot, E. R. Block, K. Bucchin, J. J. Balcita-Pedicino, M. Calderon, S. R. Sesack, A. Sorkin, Dopamine transporter localization in medial forebrain bundle axons indicates its long-range transport primarily by membrane diffusion with a limited contribution of vesicular traffic on retromer-positive compartments. *J. Neurosci.* **41**, 234–250 (2021).
30. C. Kayser, B. Melkes, C. Derieux, A. Bock, Spatiotemporal GPCR signaling illuminated by genetically encoded fluorescent biosensors. *Curr. Opin. Pharmacol.* **71**, 102384 (2023).
31. R. Yasuda, Y. Hayashi, J. W. Hell, CaMKII: A central molecular organizer of synaptic plasticity, learning and memory. *Nat. Rev. Neurosci.* **23**, 666–682 (2022).
32. L. Lin, S. Gupta, W. S. Zheng, K. Si, J. J. Zhu, Genetically encoded sensors enable micro- and nano-scopic decoding of transmission in healthy and diseased brains. *Mol. Psychiatry* **26**, 443–455 (2021).
33. L. F. Agnati, B. Bjelke, K. Fuxe, Volume transmission in the brain. *Am. Sci.* **80**, 362–373 (1992).
34. D. O. Borroto-Escuela, M. Perez De La Mora, P. Manger, M. Narváez, S. Beggiato, M. Crespo-Ramírez, G. Navarro, K. Wydra, Z. Díaz-Cabiale, A. Rivera, L. Ferraro, S. Tanganelli, M. Filip, R. Franco, K. Fuxe, Brain dopamine transmission in health and Parkinson's disease: Modulation of synaptic transmission and plasticity through volume transmission and dopamine heteroreceptors. *Front. Synaptic Neurosci.* **10**, 20 (2018).
35. B. Barbour, M. Häusser, Intersynaptic diffusion of neurotransmitter. *Trends Neurosci.* **20**, 377–384 (1997).
36. M. Sarter, V. Parikh, W. M. Howe, Phasic acetylcholine release and the volume transmission hypothesis: Time to move on. *Nat. Rev. Neurosci.* **10**, 383–390 (2009).
37. L. Descarries, B. Lemay, G. Doucet, B. Berger, Regional and laminar density of the dopamine innervation in adult rat cerebral cortex. *Neuroscience* **21**, 807–824 (1987).
38. L. Descarries, K. C. Watkins, S. Garcia, O. Bosler, G. Doucet, Dual character, asynaptic and synaptic, of the dopamine innervation in adult rat neostriatum: A quantitative autoradiographic and immunocytochemical analysis. *J. Comp. Neurol.* **375**, 167–186 (1996).
39. P. Séguéla, K. C. Watkins, L. Descarries, Ultrastructural features of dopamine axon terminals in the anteromedial and the suprarhinal cortex of adult rat. *Brain Res.* **442**, 11–22 (1988).
40. C. Missale, S. R. Nash, S. W. Robinson, M. Jaber, M. G. Caron, Dopamine receptors: From structure to function. *Physiol. Rev.* **78**, 189–225 (1998).
41. T. Yamamoto, A. Ochalski, E. L. Hertzberg, J. I. Nagy, On the organization of astrocytic gap junctions in rat brain as suggested by LM and EM immunohistochemistry of connexin43 expression. *J. Comp. Neurol.* **302**, 853–883 (1990).
42. D. R. Sibley, L. C. Mahan, I. Creese, Dopamine receptor binding on intact cells. Absence of a high-affinity agonist-receptor binding state. *Mol. Pharmacol.* **23**, 295–302 (1983).
43. E. K. Richfield, J. B. Penney, A. B. Young, Anatomical and affinity state comparisons between dopamine D1 and D2 receptors in the rat central nervous system. *Neuroscience* **30**, 767–777 (1989).
44. Ö. D. Özçete, A. Banerjee, P. S. Kaeser, Mechanisms of neuromodulatory volume transmission. *Mol. Psychiatry* **29**, 3680–3693 (2024).
45. P. F. Marcott, A. A. Mamaligas, C. P. Ford, Phasic dopamine release drives rapid activation of striatal D2-receptors. *Neuron* **84**, 164–176 (2014).
46. Z. Wu, D. Lin, Y. Li, Pushing the frontiers: Tools for monitoring neurotransmitters and neuromodulators. *Nat. Rev. Neurosci.* **23**, 257–274 (2022).
47. P. Greengard, The neurobiology of slow synaptic transmission. *Science* **294**, 1024–1030 (2001).
48. T. C. Südhof, The cell biology of synapse formation. *J. Cell Biol.* **220**, e202103052 (2021).
49. L. G. Wu, E. Hamid, W. Shin, H. C. Chiang, Exocytosis and endocytosis: Modes, functions, and coupling mechanisms. *Annu. Rev. Physiol.* **76**, 301–331 (2014).
50. H. von Gersdorff, J. G. G. Borst, Short-term plasticity at the calyx of held. *Nat. Rev. Neurosci.* **3**, 53–64 (2002).
51. C. Pulido, A. Marty, Quantal fluctuations in central mammalian synapses: Functional role of vesicular docking sites. *Physiol. Rev.* **97**, 1403–1430 (2017).
52. F. A. Edwards, A. Konnerth, B. Sakmann, Quantal analysis of inhibitory synaptic transmission in the dentate gyrus of rat hippocampal slices: A patch-clamp study. *J. Physiol.* **430**, 213–249 (1990).
53. P. Stern, F. A. Edwards, B. Sakmann, Fast and slow components of unitary EPSCs on stellate cells elicited by focal stimulation in slices of rat visual cortex. *J. Physiol.* **449**, 247–278 (1992).
54. P. Jonas, G. Major, B. Sakmann, Quantal components of unitary EPSCs at the mossy fibre synapse on CA3 pyramidal cells of rat hippocampus. *J. Physiol.* **472**, 615–663 (1993).
55. R. Malinow, R. C. Malenka, AMPA receptor trafficking and synaptic plasticity. *Annu. Rev. Neurosci.* **25**, 103–126 (2002).

56. L. Volk, S. L. Chiu, K. Sharma, R. L. Huganir, Glutamate synapses in human cognitive disorders. *Annu. Rev. Neurosci.* **38**, 127–149 (2015).
57. S. A. Connor, T. J. Siddiqui, Synapse organizers as molecular codes for synaptic plasticity. *Trends Neurosci.* **46**, 971–985 (2023).
58. J. Muir, M. Anguiano, C. K. Kim, Neuromodulator and neuropeptide sensors and probes for precise circuit interrogation in vivo. *Science* **385**, eadn6671 (2024).
59. A. S. Darvesh, R. T. Carroll, W. J. Geldenhuys, G. A. Gudelsky, J. Klein, C. K. Meshul, C. J. Van der Schyf, *In vivo* brain microdialysis: Advances in neuropsychopharmacology and drug discovery. *Expert Opin. Drug Discov.* **6**, 109–127 (2011).
60. D. L. Robinson, A. Hermans, A. T. Seipel, R. M. Wightman, Monitoring rapid chemical communication in the brain. *Chem. Rev.* **108**, 2554–2584 (2008).
61. J. Chen, K. E. Cho, D. Skwarzynska, S. Clancy, N. J. Conley, S. M. Clinton, X. Li, L. Lin, J. J. Zhu, The property-based practical applications and solutions of genetically encoded acetylcholine and monoamine sensors. *J. Neurosci.* **41**, 2318–2328 (2021).
62. M. Niello, R. Gradisch, C. J. Loland, T. Stockner, H. H. Sitte, Allosteric modulation of neurotransmitter transporters as a therapeutic strategy. *Trends Pharmacol. Sci.* **41**, 446–463 (2020).
63. R. A. Vaughan, J. D. Foster, Mechanisms of dopamine transporter regulation in normal and disease states. *Trends Pharmacol. Sci.* **34**, 489–496 (2013).
64. B. Channer, S. M. Matt, E. A. Nickoloff-Bybel, V. Pappa, Y. Agarwal, J. Wickman, P. J. Gaskill, Dopamine, immunity, and disease. *Pharmacol. Rev.* **75**, 62–158 (2023).
65. P. Song, W. Peng, V. Sauve, R. Fakih, Z. Xie, D. Ysselstein, T. Krainc, Y. C. Wong, N. E. Mencacci, J. N. Savas, D. J. Surmeier, K. Gehring, D. Krainc, Parkinson's disease-linked parkin mutation disrupts recycling of synaptic vesicles in human dopaminergic neurons. *Neuron* **111**, 3775–3788.e7 (2023).
66. J. Wang, L. M. Holt, H. H. Huang, S. R. Sesack, E. J. Nestler, Y. Dong, Astrocytes in cocaine addiction and beyond. *Mol. Psychiatry* **27**, 652–668 (2022).
67. C. Lüscher, V. Pascoli, 'Ups, downs, and sideways' of dopamine in drug addiction. *Trends Neurosci.* **44**, 593–594 (2021).
68. Y. Zhuo, B. Luo, X. Yi, H. Dong, X. Miao, J. Wan, J. T. Williams, M. G. Campbell, R. Cai, T. Qian, F. Li, S. J. Weber, L. Wang, B. Li, Y. Wei, G. Li, H. Wang, Y. Zheng, Y. Zhao, M. E. Wolf, Y. Zhu, M. Watabe-Uchida, Y. Li, Improved green and red GRAB sensors for monitoring dopaminergic activity in vivo. *Nat. Methods* **21**, 680–691 (2024).
69. M. Jing, P. Zhang, G. Wang, J. Feng, L. Mesik, J. Zeng, H. Jiang, S. Wang, J. C. Looby, N. A. Guagliardo, L. W. Langma, J. Lu, Y. Zuo, D. A. Talmage, L. W. Role, P. Q. Barrett, L. I. Zhang, M. Luo, Y. Song, J. J. Zhu, Y. Li, A genetically encoded fluorescent acetylcholine indicator for *in vitro* and *in vivo* studies. *Nat. Biotechnol.* **36**, 726–737 (2018).
70. K. T. Beier, E. E. Steinberg, K. E. DeLoach, S. Xie, K. Miyamichi, L. Schwarz, X. J. Gao, E. J. Kremer, R. C. Malenka, L. Luo, Circuit architecture of VTA dopamine neurons revealed by systematic input-output mapping. *Cell* **162**, 622–634 (2015).
71. A. T. Popescu, M. R. Zhou, M. M. Poo, Phasic dopamine release in the medial prefrontal cortex enhances stimulus discrimination. *Proc. Natl. Acad. Sci. U.S.A.* **113**, E3169–E3176 (2016).
72. G. Wang, P. Zhang, S. K. Mendu, Y. Wang, Y. Zhang, X. Kang, B. N. Desai, J. J. Zhu, Revaluation of magnetic properties of Magneto. *Nat. Neurosci.* **23**, 1047–1050 (2020).
73. L. Huang, Y. Chen, S. Jin, L. Lin, S. Duan, K. Si, W. Gong, J. J. Zhu, Organizational principles of amygdalar input-output neuronal circuits. *Mol. Psychiatry* **26**, 7118–7129 (2021).
74. C. Liu, X. Cai, A. Ritzau-Jost, P. F. Kramer, Y. Li, Z. M. Khaliq, S. Hallermann, P. S. Kaeser, An action potential initiation mechanism in distal axons for the control of dopamine release. *Science* **375**, 1378–1385 (2022).
75. J. Ding, J. N. Guzman, T. Tkatch, S. Chen, J. A. Goldberg, P. J. Ebert, P. Levitt, C. J. Wilson, H. E. Hamm, D. J. Surmeier, RGS4-dependent attenuation of M4 autoreceptor function in striatal cholinergic interneurons following dopamine depletion. *Nat. Neurosci.* **9**, 832–842 (2006).
76. G. Wang, D. R. Wyskiel, W. Yang, Y. Wang, L. C. Milbern, T. Lalanne, X. Jiang, Y. Shen, Q.-Q. Sun, J. J. Zhu, An optogenetics- and imaging-assisted simultaneous multiple patch-clamp recording system for decoding complex neural circuits. *Nat. Protoc.* **10**, 397–412 (2015).
77. J. J. Zhu, Architectural organization of ~1,500-neuron modular minicolumnar disinhibitory circuits in healthy and Alzheimer's cortices. *Cell Rep.* **42**, 112904 (2023).
78. M. Arigovindan, J. C. Fung, D. Elnatan, V. Mennella, Y.-H. M. Chan, M. Pollard, E. Branlund, J. W. Sedat, D. A. Agard, High-resolution restoration of 3D structures from widefield images with extreme low signal-to-noise-ratio. *Proc. Natl. Acad. Sci. U.S.A.* **110**, 17344–17349 (2013).
79. E. Wernersson, E. Gelali, G. Girelli, S. Wang, D. Castillo, C. Mattsson Langseth, Q. Verron, H. Q. Nguyen, S. Chattoraj, A. Martinez Casals, H. Blom, E. Lundberg, M. Nilsson, M. A. Marti-Renom, C. T. Wu, N. Crosetto, M. Bienko, Deconwolf enables high-performance deconvolution of widefield fluorescence microscopy images. *Nat. Methods* **21**, 1245–1256 (2024).

Acknowledgments: We thank members of the J. J. Zhu laboratory for suggestions and technical assistance. We thank J. J. Zhu for guidance on this project. **Funding:** This work was supported, in part, by NIH R01NS121014, the Owens Family Foundation, the Brain Institute, the 3 Cavaliers Research Award, and the Presidential Fellowship for Collaborative Neuroscience from the University of Virginia. **Author contributions:** L.H. and B.J.V. led the project with input from W.J.L. L.H. and Y.C. performed the experiments. L.H. and Y.C. analyzed the data with assistance from Z.Y. **Competing interests:** The authors declare that they have no competing interests. **Data and materials availability:** All data needed to evaluate the conclusions in the paper are present in the paper and/or the Supplementary Materials. All data presented in the figures are available at the University of Virginia's Libra database (https://doi.org/10.18130/V3/KOMDZU).

Submitted 21 March 2025
Accepted 24 April 2025
Published 28 May 2025
10.1126/sciadv.adx6367